IEEE Access
Multidisciplinary | Rapid Review | Open Access Journal

Received November 15, 2021, accepted December 11, 2021, date of publication December 20, 2021,
date of current version December 28, 2021.

Digital Object Identifier 10.1109/ACCESS.2021.3136779

Development of a Balanced 3D Translational Interconnected Manipulator With Solely Rotary Joints/Actuators and Free-Internal-Singularity Workspace

AHMED SAMEH[1], MOHAMED FANNI[1,2], VICTOR PARQUE[1,3], (Member, IEEE), AND ABDELFATAH M. MOHAMED[1,4], (Life Senior Member, IEEE)

[1]Mechatronics and Robotics Engineering Department, Egypt-Japan University of Science and Technology (E-JUST), New Borg El-Arab, Alexandria 21934, Egypt
[2]Production Engineering and Mechanical Design Department, Faculty of Engineering, Mansoura University, Mansoura 35516, Egypt
[3]Department of Modern Mechanical Engineering, Waseda University, Shinjuku, Tokyo 169-8555, Japan
[4]Electrical Engineering Department, Faculty of Engineering, Assiut University, Assiut 71516, Egypt

Corresponding author: Ahmed Sameh (ahmed.ismaeil@ejust.edu.eg)

This work was supported in part by the Egypt–Japan University of Science and Technology (E-JUST) of manufacturing the manipulator prototype together with Agro-Food Alliance, and in part by Waseda University. The work of Ahmed Sameh was supported by the Ministry of Higher Education of Egypt.

ABSTRACT A new interconnected translational manipulator is proposed. It is the only interconnected manipulator that makes such motion using revolute joints and three rotary actuators. Rotary joints and actuators are favored practically than their linear counterparts due to their lower price, lower size of installation and higher reliability. The configuration of the proposed manipulator allows it to maintain, to a large extent, the combined merits of serial and parallel manipulators. In contrast to all other existing interconnected manipulators, the proposed manipulator has free-internal-singularity workspace. Using a practical proposed methodology, a balancing system is developed that reduces dramatically the power consumption and facilitates using small-sized-motors. The mobility analysis is carried out using a newly developed methodology suitable for interconnected manipulators. Closed forms for position and velocity kinematics as well as for maximum cuboid workspace are derived. The developed mechanical design is validated by finite element analysis. The controller performance is tested using ADAMS® & MATLAB®/Simulink co-simulation. The results indicate the feasibility of the proposed manipulator and its advantages over existing translational manipulators from engineering as well as economic viewpoints.

INDEX TERMS Industrial manipulator, translational motion, rotary actuators, kinematic analysis, free-internal singularities, balance.

I. INTRODUCTION

Triggered by recent drivers in technology transformation inducing the Fourth Industrial Revolution, robot manipulators have attracted the attention in enabling the cost-effective and the energy-efficient packaging, sorting, picking, placing, assembling, welding, painting and other practical general-purpose tasks. As such, classifying robot manipulators into manipulators of serial and parallel nature has been a usual practice [1]. Basically, serial manipulators comprise consecutively joined links whose active joints are generally driven by rotary actuators fixed on the links; and due to such structure, serial manipulators are well-known for their superior workspace to size ratio [2].

Conversely, parallel manipulators connect the end-effector to the ground through several independent chains with actuators mounted concurrently near/at the fixed platform. Due to loads being distributed, links being able to be light, and the nature of concurrent coupling, parallel manipulators can enable less body inertia, high structural rigidity, high dexterity, high operational speed and superior positioning accuracy [1]. The above-mentioned makes parallel manipulators appealing for a number of practical scenarios requiring superior precision, speed, and stiffness; and the last decades have rendered favorable interest in this direction [3]–[7].

In line with the above, several general-purpose manipulations in industrial settings require that the end-effector

The associate editor coordinating the review of this manuscript and approving it for publication was Guilin Yang.

not only move in translational motions in the Cartesian *x-y-z* domain, but also keep the orientation constant. This problem is suitable to the application of parallel manipulators, rather than serial schemes, such as the Tsai structure [8], the Delta robot [9], [10] with 3 degrees of freedom (DOF) - using revolute joints (rotary actuators), and the orthoglide robot with linear joints mounted orthogonally [11]. Although other manipulator architectures achieving pure translational motions were also proposed, such as the 3-UPU platform [12], 3-RUU (3-PUU) mechanisms [13], the 3-CRR manipulator [14], the 3-RPC architecture [15], the 3-PUU with 2 rotational DOFs and 1 translational DOFs (2R1T) [16], [17] in which R, P, U, C, and S denote revolute, prismatic, universal, cylindrical, and spherical joints, respectively.

Through a US patent in May 2001, Gosselin and Kong proposed a 3 DOF parallel manipulator with decoupled input-output equations [18]; and in subsequent years, extended architectures were proposed, such as

- The Tripteron [19], [20].
- The Pantopteron using three pantograph linkages [21].
- Quadrupteron with 3 independent translations and 1 rotation around an axis with fixed direction (3T1R), or Schönflies motions, and whose structure was synthesised by evolutionary computing [22].
- The Isoglide4 [23].
- The Pantopteron-4 (3T1R) using three pantograph linkages and Schönflies motions enabling faster displacement than Isoglide4 or the Quadrupteron [24].
- The Tri-pyramid robot with the triangular pyramidal constraint [25], [26].
- The decoupled pantograph manipulator with three translational degrees of freedom which belongs to a recently introduced family of industrial robots named interconnected manipulators [27], [28].

The above-mentioned studies introduced novel mechanisms with faster and highly accurate positioning of the end effector while keeping the workspace as large as possible to allow the extended dexterity in manipulation tasks. Also, among the above-mentioned decoupled translational manipulators, the manipulator using pantograph linkages is potential to increase the workspace-to-size ratio, comparable to that of serial manipulators, due to its cantilever-like-configuration. Also, since actuators are located near/at the base, similar to the configuration of parallel manipulators, their links can be made light weight, implying high rigidity, high-speed and accurate operations. However, despite these advantages of this novel design [27], [28], it has workspace limitations as it uses three linear actuators with small strokes that reduces the available workspace. Furthermore, the linear actuators in [27] and [28] are more expensive and less reliable compared with rotary actuators. In addition, the structure in [27] and [28] has internal singularities that decrease the available workspace further. Conversely, the 3-parallelogram lightweight robotic arm proposed by Wu *et al.* [29] has translational motions in two orthogonal directions and one rotational motion along the third orthogonal direction, allowing the use of three rotary actuators; yet its structure presents internal singularities in the workspace. Another example of an interconnected manipulator, oriented towards pick-and-place operations, is the Robocombi® [30] which uses one linear actuator, with a large stroke, and two rotary actuators. However, besides using linear actuators, this robot also presents internal singularities like the conventional manipulators in the literature.

Several designs of hybrid robots have been presented with a detailed study of their performance analysis, structure synthesis and applications, but they still have some limitations regarding workspace volume and singularities [31]–[35]. In the best of the author's knowledge, there exists no 3D translational manipulator that uses solely revolute joints and rotary actuators, although it is highly desirable for practical considerations in industrial tasks. The authors filled this gap by proposing such needed manipulator in [36]; however, this proposed manipulator suffers from internal singularities that reduce the available workspace. These singularities are similar to those observed in the manipulator [27], [28]. Thus, having received little favorable attention in the community, the study of interconnected manipulators being free of internal singularities and using only revolute joints has the potential to expand the frontiers in cost-efficiency and maneuverability. Indeed, revolute joints and three rotary actuators are more favorable than their linear counterparts due to their lower price, lower size of installation and higher reliability. In this paper, to fill this gap, we propose a pantograph-based interconnected manipulator and study its properties. In particular, our contributions are as follows:

- A unique 3D translational manipulator by using only revolute joints and three rotary actuators, whose topology is free of internal singularities.
- The mobility analysis, using a suitable method to address the configuration of interconnected kinematic mechanisms with geometric constraints, sketched the velocity diagrams in 3D domain, and identified the directions of the linear and the angular velocities of the end-effector. We also explored the kinematics, the workspace, and the largest cuboid in the workspace in 3D domain analytically. We found that the size of the workspace of the proposed manipulator is 3 (9) times larger than that of the 3D pantograph (Pantopteron) manipulator.
- The computational analysis based on finite element analysis have shown that a potentially manufacturable structure is safe from the viewpoints of stress and deformation under a 5kg payload. And, a tailored balancing system has shown to significantly reduce the required torque in the rotary (motor) actuators by a factor of 234 and 512 times, implying the reduced size and power consumption of required motors.
- Furthermore, the computational simulation experiments based on the co-simulation between MATLAB® (Simulink) and ADAMS® have shown the feasibility of using simple PID control schemes to attain

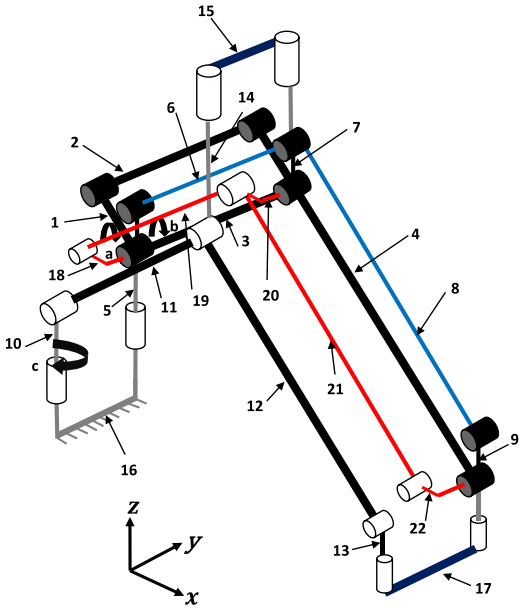

FIGURE 1. A schematic diagram of the proposed manipulator.

high-performing trajectory tracking of the end-effector and the joint angles.

In the following sections we describe our proposed approach, analysis and outline our conclusions.

II. DESCRIPTION OF THE PROPOSED MANIPULATOR

The basic scheme of the proposed manipulator is shown by Fig. 1 in which links are labeled with numbers from 1 to 22, actuators (motors) are labeled with letters **a**, **b** and **c**. Also, the base is fixed and labeled with number 16 and is gray color, and the end effector is labeled with number 17 and is blue-colored (Fig. 1). Furthermore, by observing Fig. 1, we note the following features:

- The proposed manipulator comprises seven parallelograms that make the end-effector achieve translational motions in 3D domain while being free of internal singularities. Here, due to the configuration of links in Fig. 1, there exists 5 parallelograms comprising (1,2,3,4), (5,6,7,3), (7,8,9,4), (18,19,20,3) and (20,21,22,4) whose planes are parallel among each other. Also, there exists 2 parallelograms comprising (16,11,15,3) and (15,12,17,4) whose planes are orthogonal to the 5 parallelograms mentioned above.
- Three rotary actuators located near the fixed base (label 16 in Fig. 1) enable the translational motions of the end-effector. Here, motors **a** and **b** enable the motion in x and z axes, while motor **c** along with motors **a** and **b** allow for motion in the y-axis.
- Parallelogram with links (1,2,3,4) is considered the main parallelogram as the rotary actuators **a** and **b** are attached at links 1 and 3. This parallelogram is responsible for moving the end-effector in two directions only x and z.
- Parallelograms with links (5,6,7,3), (7,8,9,4) are responsible for fixing the orientation of the end-effector (17 in Fig. 1) while moving in x and z axes.
- The two Parallelograms with links (16,11,15,3) and (15,12,17,4) are responsible for moving the end-effector in y axis with a fixed orientation.

So, by using these 5 parallelograms, the end-effector can move 3D translational motions with fixed orientation in x, y and z.

- Parallelograms with links (18,19,20,3) and (20,21,22,4) are responsible for eliminating the internal singularities in the available workspace. These two parallelograms have common links with the two parallelograms (5,6,7,3) and (7,8,9,4). Link (3) is common between (18,19,20,3) and (5,6,7,3) while link (4) is common between (20,21,22,4) and (7,8,9,4).
- Link (18) is rigidly attached and perpendicular to link (5), link (20) is rigidly attached and perpendicular to link (7), and link (18) is rigidly attached and perpendicular to link (5). This 90^{o} shift between the links of the connected parallelograms guarantees passing through the singularity configurations without damaging the parallelism of the parallelogram links. If one parallelogram is in a singular configuration (all its links are aligned), the internal angles between the links of its connected parallelogram are 90^{o} which forces the parallelism of the parallelograms' links in the subsequent motion and hence avoids kinematic bifurcation at the singular position. A rigorous proof to eliminate the internal singularities using these two parallelograms will be explained in section III.
- The parallelograms (16,11,15,3), (15,12,17,4), (1,2,3,4), (5,6,7,3) and (7,8,9,4) facilitate the movement of the end-effector in the y direction controlled by motor **c**, without changing the orientation in the horizontal plane.
- The parallelism and orthogonality of the parallelograms' working planes play an essential role to enable the seamless coverage of the workspace while avoiding kinematic bifurcations at singularities.

The CAD model for the proposed manipulator with its balancing springs are shown in Fig. 2. The balancing system will be presented in section VI.

III. MOBILITY ANALYSIS

The general Grubler-Kutzback formula is known to be used to calculate the number of degrees of freedom (DOF) which can be represented as follows:

$$F = \lambda\,(n - j - 1) + \sum_{i=1}^{j} f_i \tag{1}$$

where F stands for the number of DOF, n represents the number of links, j stands for the number of joints, λ represents the workspace dimension and f_i is the DOF of joint i. The DOF of the suggested manipulator is obtained as:

$$F = 6(17 - 21 - 1) + 21 = -9 \tag{2}$$

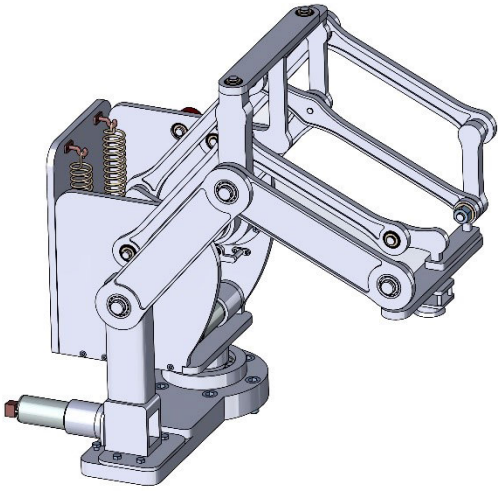

FIGURE 2. The CAD model of the proposed manipulator.

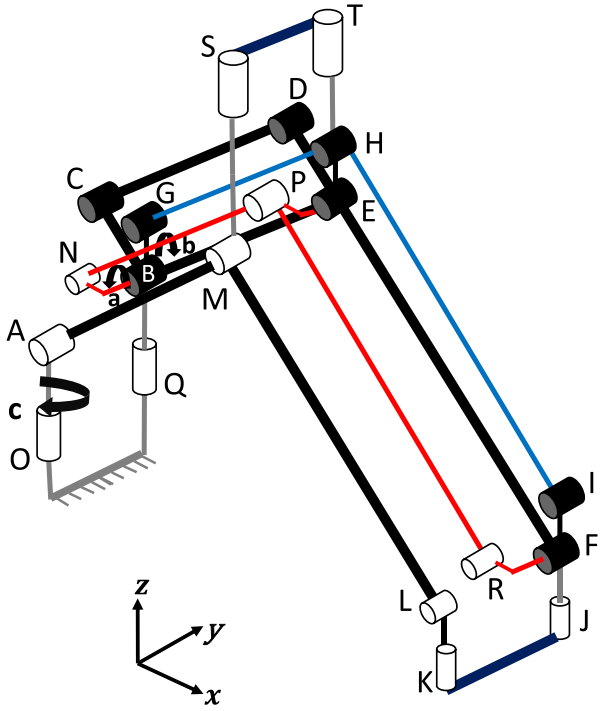

FIGURE 3. Schematic diagram of the proposed manipulator showing labels of joints and links to be used in sketching the three-dimensional velocity diagram.

It is to be noted that neither links (19) and (21) (shown in Fig. 1) nor joints N, P, and R (shown in Fig. 3) are counted in Eq. (2). This is because they belong to the redundant parallelograms (18,19,20,3) and (20,21,22,4) which are responsible for eliminating the internal singularities as mentioned in section II.

The negative number resulted from Eq. (2) indicates that the suggested manipulator is a fixed structure without any ability to move in the 3D space. It is well recognized that the formula of Grubler fails in cases of mechanisms/manipulators possess unique geometry such as Delta and Tsai manipulators [8]–[10]. The suggested manipulator in this paper possesses also a unique geometry which enables it to move. As illustrated previously in Figs. 1 and 2, the unique geometry is introduced by the parallelism of the two vertical planes containing the vertical axes of the joints O, Q, S, T, K, and J (shown in Fig. 3) as well as the length equality of the opposite links of the parallelograms.

So, another mobility method is needed not only for calculating the number of DOF but additionally for defining the motion's type, singularity configurations and the actuators' locations. Recently, an innovative method is proposed by the authors [27] to obtain the mobility information of hybrid manipulators where other mobility methods failed to obtain such information because of the non-serial non-parallel nature of the kinematic chains of the interconnected manipulators. This new method is based on sketching 3D velocity diagram of the interconnecting manipulators. The idea behind sketching (not scale drawing) of the 3D velocity diagram is that the twist system of the end-effector can be identified through the directions of linear and angular velocities (not magnitudes) of the end-effector. Knowing such twist (or wrench) system, the mobility information can be obtained. Sketching 3D velocity diagrams provides us with the needed information about the directions (not the magnitude) of the end-effector's linear and angular velocities. In [27], the rules of sketching (drawing) 3D velocity diagrams as well as the guidelines to extract the mobility information are introduced.

A. SKETCHING THE THREE-DIMENSIONAL VELOCITY DIAGRAM

By applying the rules in [27], the velocity diagram in the 3D space for the suggested manipulator can be sketched as illustrated in Fig. 4. The schematic diagram of the manipulator showing the concerned points is illustrated in Fig. 3. The sketch starts with drawing points o and q which represent the fixed points O and Q. points o and q are called the origin of the velocity diagram. Then points, a, b, and g are coincident with points o and q since they are located on the axis of rotation of revolute joints attached to the ground. If the actuator c is located at Q instead of being at O, the linear velocity of point C can be estimated. However, we will assume that joint Q has a known angular velocity. While continue drawing the three-dimensional velocity diagram, the actual angular velocity of joint Q will be revealed which justifies the sketch.

$$\vec{v}_C = \vec{\omega}_{BC} \times \overline{BC} \tag{3}$$

Since there are two revolute joints (located at points Q and B) connecting link BC with the ground, $\vec{\omega}_{BC}$ has two components: $\dot{\varphi}$ in the vertical direction and $\dot{\theta}_2$ in a direction orthogonal to the plane of the parallelogram BCDE.

Hereafter,

$$\vec{v}_C = \vec{\dot{\varphi}} \times \overline{BC} + \dot{\theta}_2 \times \overline{BC} \tag{4}$$

Since, the magnitude and direction of each vector in the right-hand side is known ($\vec{\dot{\theta}}_2$ is the angular velocity of motor **a**, and we assumed $\vec{\dot{\varphi}}$ to be known), we can draw the two components of $\vec{v}_C$. From the velocity diagram origin, we draw $\vec{\dot{\theta}}_2 \times \overline{BC}$ as a line perpendicular to BC and parallel to the parallelogram BCDE following the direction sense of $\vec{\dot{\theta}}_2 \times \overline{BC}$. The end of this line is labelled $\grave{c}$.

From $\grave{c}$, we draw a line perpendicular to the parallelogram BCDE following the direction sense of $\vec{\dot{\varphi}} \times \overline{BC}$. The end of this line is labelled c. Similarly,

$$\vec{v}_E = \vec{\dot{\varphi}} \times \overline{\boldsymbol{BE}} + \vec{\dot{\theta}}_1 \times \overline{\boldsymbol{BE}} \tag{5}$$

where $\vec{\dot{\theta}}_1$ is the angular velocity of motor **b**. So, point $\grave{e}$ can be located at the end of the component $\vec{\dot{\theta}}_1 \times \overline{\boldsymbol{BE}}$ and e at the end of the followed component $\vec{\dot{\varphi}} \times \overline{\boldsymbol{BE}}$. Using the parallelogram rule [27], points d and h can also be located (BCDE and BGHE are parallelograms and represented by parallelograms bcde and bghe in the 3D velocity diagram).

It is to be noted that h coincides with e since g coincides with b. Using proportion rule [27], point t coincides also with h and e. It is to be noted that φ, θ_1 and θ_2 are the angular rotations of the revolute joints at Q and B as shown in Fig. 5. Also, $\mathbb{a}$ and $\mathbb{b}$ are the lengths of the parallelogram sides as shown in Fig. 5.

It is important to highlight that OA, AM, MS, ML and LK are equal to QB, BE, ET, EF and FJ respectively. Initially, the manipulator is set up with the two links of each pair above are parallel. Proving the validity of these parallelisms for any subsequent motion is one of the goals in our mobility analysis. Also, OQ, ST and KJ have the same length and are set up initially to be parallel. Proving the parallelism of these links for any subsequent motion will be considered later. It is important to highlight that all points on a revolute joint axis belong to the two links connected by this joint. Point M is on the vertical axes of the revolute joints connecting links TS with SM and SM with MA. Then, M can be considered belongs to links AM, MS and ST. Likewise, point E is considered belongs to links ST, TE and EB.

Thus, points M and E belong to the same link ST and hence the distance between them is constant. Since SM and TE have the same length and parallel to each other, then ST and ME have the same length and parallel to each other. Using similar approach, one can verify that AB and OQ have the same length and parallel to each other.

The next point to be found is point M. Since the three collinear points T, H, and E, which are located on the revolute joint axis at T, are represented in the three-dimensional velocity diagram by the same point, the axis EHT does not change its direction and its only possible rotation is about itself. Hence, the angular velocity direction of ST, if existing, will be a long line EHT. Since $\vec{\omega}_{ST}$ is parallel to the Z-axis and, as initially set, ST is parallel to the Y-axis, then $\vec{v}_{ME}$ is parallel to the X-axis, and hence, parallel to the horizontal plane XY. From point e in the three-dimensional velocity diagram, one draws a line parallel to the X-axis which is the first m-line. It is to be noted that $\vec{v}_{MA}$ which equal to $\vec{v}_M$, has two components, since link AM is connected to the ground through a serial chain having two revolute joints at A and O.

One component starts at the velocity diagram origin and is orthogonal to AM and parallel to the BCDE-parallelogram plane, i.e. $\grave{m}$ is located on the line o$\grave{e}$. The other component starts at $\grave{m}$ and is orthogonal to the BCDE-parallelogram plane i.e. parallel to the horizontal plane XY. So, the second m-line should start at a point $\grave{m}$ on the line o$\grave{e}$ and be parallel to XY plane. Hence, the two m-lines are parallel to the same plane. Consequently, the only solution is that the two m-lines are located on the same horizontal plane so they can intersect each other. The first m-line is located on a horizontal plane formed by itself and the line e$\grave{e}$ (e$\grave{e}$ is orthogonal to BCDE-parallelogram plane i.e. parallel to the horizontal plane). Therefore, the only possibility of the intersection of the two m-lines is that $\grave{m}$ coincides with $\grave{e}$. Consequently, the second m-line coincides with e$\grave{e}$ line and intersect the first m-line at point e. Hence m coincides with e and t.

Since, M, E and T are 3 non-collinear points on link STEM, link STEM is a translational link. This proves the parallelism of both BA and EM for subsequent motion. Also, they are equal then, the parallelism of AM and BE for subsequent motion is also proved. Consequently, the angular velocities of AM and BE are equal which is also obvious from the 3D velocity diagram. Since the components of $\vec{v}_E$ are equal to those of $\vec{v}_M$, then the joints' angular velocities of O and A are equal to those of Q and B respectively. Subsequently, the assumed joint's angular velocity at Q is revealed to be equal to the angular velocity of motor c.

Using the proportion rule, point f can be found through extending line de. Since EHIF is a parallelogram and points e, h and f are already found where $\vec{v}_E$ is equal to $\vec{v}_H$, then according to the parallelogram rule [27], point i coincides with point f. Since, points J, F and I are 3 collinear points on the same link where points f and i coincide on each other, then j coincides also with f and i according to the proportion rule. Since the three collinear points J, F, and I, which are located on the revolute joint axis at J, are represented in the three-dimensional velocity diagram by the same point, the angular velocity direction of J K, if existing, will be a long line J F I. As previously noted, links J K and ST have the same length and are initially parallel to each other. Since $\vec{\omega}_{JK}$ is parallel to the Z-axis and, as initially set, J K is parallel to the Y-axis, then $\vec{v}_{LF}$ is parallel to the X-axis, and hence, parallel to the horizontal plane XY.

From point f in the three-dimensional velocity diagram, one draws a line parallel to the X-axis which is the first l-line. It is to be noted that $\vec{v}_{LM}$ has three components, since link LM is connected to the ground through a serial chain having

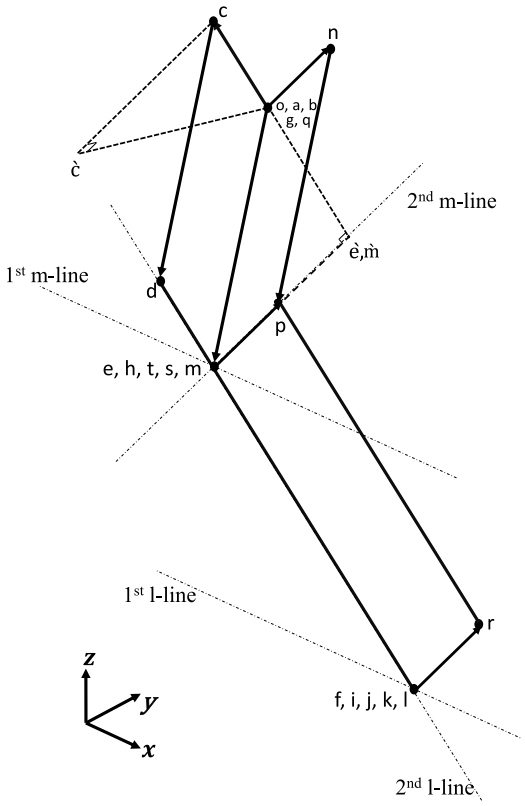

FIGURE 4. The three-dimensional velocity diagram of the proposed manipulator.

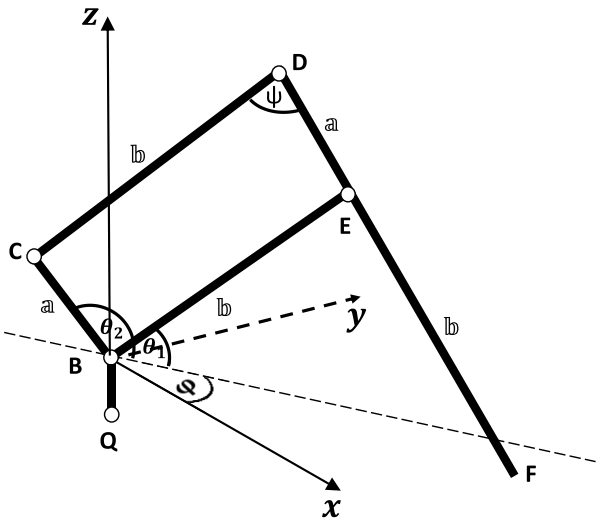

FIGURE 5. The main parallelogram of the manipulator.

three revolute joints at M, A and O. Keeping in mind that L M and FE have the same length and are initially parallel to each other in addition to the permanent parallelism between OA and QB and between AM and BE, the first two components of $\vec{v}_{LM}$ corresponding to the rotations at O and A and the corresponding components of $\vec{v}_{FE}$ are equal to each other. Also, the third components of $\vec{v}_{LM}$ and $\vec{v}_{FE}$ are in the same direction. From point e in the three-dimensional velocity diagram, one draws the three components of $\vec{v}_{FE}$ that end at point f. From point m, which is coinciding with point e, the first two components of $\vec{v}_{LM}$, which are coinciding with the first two components of $\vec{v}_{FE}$, are drawn. Then, from the end point of the first two components of $\vec{v}_{LM}$, one draws the second l -line which represents the third component of $\vec{v}_{LM}$. The direction of this line coincides with the direction of the third component of $\vec{v}_{FE}$.

It is obvious that point f is the intersection point of the two l-lines. Since the three collinear points F, J, and L which belong to link J K are representing by one point in the three-dimensional velocity diagram, then link J K is a translational link. This proves the parallelism between J K and S T and between L M and F E. Point k coincides with l, j, f and i points.

Now, we will find the points n, p and r that represent the points located on the redundant parallelograms (18,19,20,3) and (20,21,22,4) responsible for eliminating the interior singularities from the workspace. It is to be noted that the horizontal link NB is rigidly attached with the vertical link QBG which rotates with $\dot{\vec{\varphi}}$ around itself. Accordingly, the direction of $\vec{v}_N$ is perpendicular to the plane QBGN and its magnitude is the length NB multiplied by $\dot{\vec{\varphi}}$. So, point n is located in the 3D velocity diagram. Since BNPE forms a parallelogram where its three points b, n, and e are already located in the three-dimensional velocity diagram, the fourth point p can be located using the parallelogram rule [27]. Similarly, point r can be located using the parallelogram rule (three points e, f, and p belong to the parallelogram EFRP are already located in the 3D velocity diagram).

B. INFERENCE OF MOBILITY INFORMATION

C. VALIDATING ACTUATORS' LOCATIONS

It is clear from section III (A) that the three-dimensional velocity diagram of the proposed manipulator is uniquely defined for arbitrary configurations except for limited cases such as when a parallelogram degenerates into a line and thus the parallelogram rule cannot be applied. Therefore, the three rotary actuators presented are valid for manipulator actuation.

D. DEDUCTING SINGULAR CONFIGURATIONS

The singular configurations of the manipulator where the three-dimensional velocity diagram could not be defined are as follows:

- $\theta_1 = \theta_2 = 90°$ and $\varphi = 0°$. At this configuration, the parallelogram BCDE degenerates into a vertical line at the boundary of the workspace.
- $\theta_2 - \theta_1 = 180°$ (or $\psi = 180°$ in Fig. 5). At this configuration, the parallelogram BCDE degenerates into a line where the end-effector is at the boundary of the workspace.
- $\varphi = \pm 90°$. This occurs when the two m-lines (see Fig. 4) are aligned. In such a case, one can not specify an

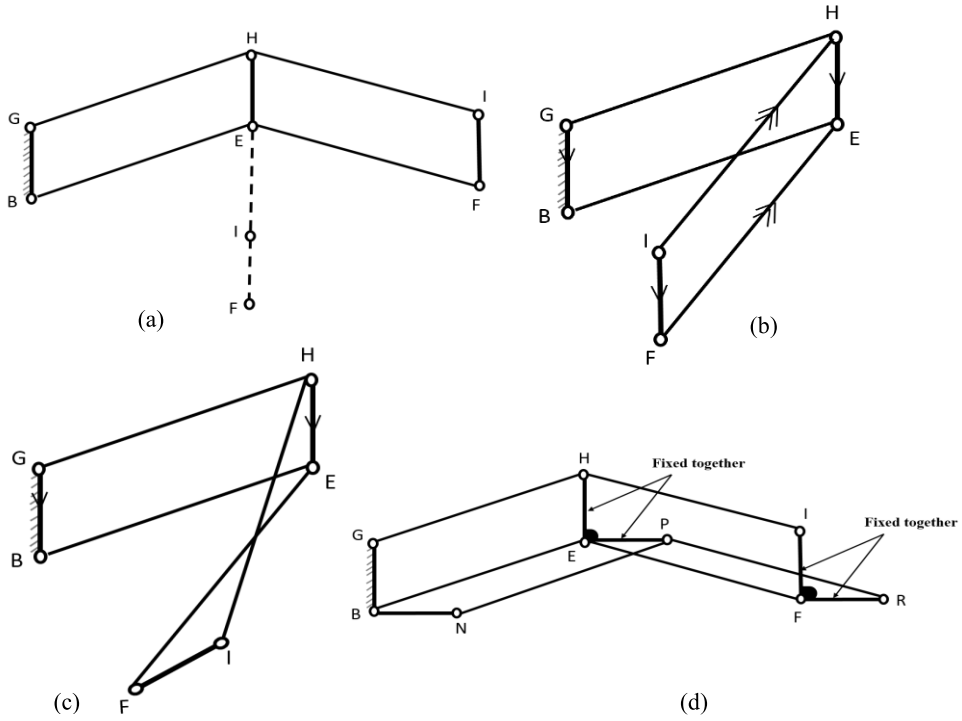

FIGURE 6. Explaining of the Internal Singularities in the previous design [36] as shown at figures (a), (b) and (c). The additional parallelograms that were added to eliminate internal singularities are shown in figure (d).

intersection point of the two m-lines, and hence the three-dimensional velocity diagram cannot be defined. This occurs when the BCDE-parallelogram plane be orthogonal to the X-axis.

The internal singularity in the original design [36] exists when the parallelograms of the guiding mechanisms are degenerated into lines as shown in figure 6 (a). At these configurations, there is no control on the direction of rotation of the opposite link to the fixed one. It can continue the rotation normally parallel to its opposite link as shown in figure 6 (b) or continue the rotation non parallel to the opposite link as shown in figure 6 (c). The last case results in changing the orientation of the end-effector and hence destroys the main characteristic of the proposed manipulator namely the fixed orientation of the end-effector.

In order to overcome this problem, we add an additional similar parallelogram such that one moving link of one parallelogram is rigidly fixed to the corresponding link of the other parallelogram and makes angle 90° with it as shown in figure 6 (d). Now if one parallelogram becomes in a singular configuration, the other parallelogram becomes in the farthest position away from the singularity position and guides the first one to come out from the singularity position with parallel links.

E. MOTION TYPE

As shown in section III(A), points F, J, and L which belong to the end-effector and are not located on the same line are represented in the three-dimensional velocity diagram by one point. This occurs for arbitrary non-singular configurations as well as for arbitrary input velocities. Therefore, the full-cycle translational motion of the end-effector has been proved [27].

F. NUMBER OF DEGREES OF FREEDOM

The number of DOF can be determined using the linear velocity vector of one point, F, located on the end-effector which possesses translation motion as proved above.

Now, it is needed to determine the linear dependence/independence of the three components of $\vec{v}_F$. This can be accomplished easily by relating the velocity of point F to that of point E (see Figs. 4 and 5)) as follows:

$$\vec{v}_F = \vec{v}_E + \vec{v}_{FE} = \vec{\dot{\varphi}} \times \overline{\boldsymbol{BE}} + \vec{\dot{\theta}}_1 \times \overline{\boldsymbol{BE}} + \vec{\dot{\varphi}} \times \overline{\boldsymbol{EF}} + \vec{\dot{\theta}}_1 \times \overline{\boldsymbol{EF}} + (\vec{\dot{\theta}}_2 - \vec{\dot{\theta}}_1) \times \overline{\boldsymbol{EF}} = \vec{\dot{\varphi}} \times \left(\overline{\boldsymbol{BE}} + \overline{\boldsymbol{EF}}\right) + \vec{\dot{\theta}}_1 \times \overline{\boldsymbol{BE}} + \vec{\dot{\theta}}_2 \times \overline{\boldsymbol{EF}} \tag{6}$$

One can show that the above three components of $\vec{v}_F$ are indeed independent components as follows. The direction of the first component is orthogonal to the plane of the parallelogram BCDE while the second and third components are parallel to it. The second component is perpendicular to $\overline{\boldsymbol{BE}}$ and the third component is perpendicular to $\overline{\boldsymbol{EF}}$.

Thus, the three directions of these three components are linearly independent for all non-singular configurations and can be a basis of the 3D space. Moreover, the magnitude of each component is function of only one motor speed i.e. independent of each other. Since the three components are

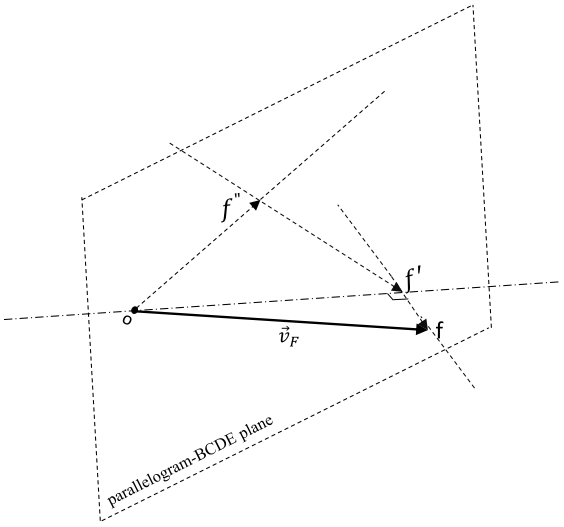

FIGURE 7. The 3D sketch of the three components of the end-effector's velocity.

independent, the DOF is three. It is worth to visualize these three components and show how to get the motors' angular-velocities corresponding to arbitrary end-effector velocity through sketching a simple 3D-VD as indicated in Fig. 7. One draws the vector of arbitrary $\vec{v}_F$ from the origin, o. The end of this vector is point f. From f, one draws a line orthogonal to the parallelogram-BCDE plane. This line intersects a plane, which is parallel to the parallelogram-BCDE plane and passing through point o, at point $f^{'}$. From o and $f^{'}$, one draws two lines parallel to the parallelogram-BCDE plane. One line is perpendicular to $\overline{\boldsymbol{BE}}$ and the other is perpendicular to $\overline{\boldsymbol{EF}}$. The two lines intersect at $f^{''}$.

The three components of $\vec{v}_F$ are $of^{''}$, $f^{''}f^{'}$ and $f^{'}f$. Through simple geometrical relations obtained from the 3D-VD sketch, one can get the magnitudes of these components as function of the magnitude of $\vec{v}_F$.

Comparing the obtained magnitudes and directions of these components with the corresponding magnitudes' expressions and directions of these components in Eq. (6), one can easily obtain $\vec{\dot{\varphi}}$, $\vec{\dot{\theta}}_1$, and $\vec{\dot{\theta}}_2$.

This 3D geometrical approach is far simpler than the traditional approach using the inverse of Jacobian which will be presented in the next section. This example indicates clearly the key idea of our mobility analysis which is based on 3D geometrical approach. The 3D geometrical approach enables us to get full mobility information for interconnected manipulators using simple sketch where other methodologies fail. To get expression for the end-effector twist using analytical approach is too complicated and it is almost impossible to extract mobility information from it.

IV. KINEMATIC ANALYSIS

A. FORWARD KINEMATIC ANALYSIS

Kinematic analysis of the proposed hybrid manipulator is assumed to be an essential step that relates the end-effector's position with the input variables. As shown in the previous section, the end-effector has 3D translational motion. So, it is enough to carry out the forward/inverse kinematics using the position of one point on the end-effector. The position vector of point F on the end-effector with respect to the fixed frame {o-xyz} as displayed in Fig. 4, is represented as $\boldsymbol{P_f} = \left[x_f, y_f, z_f\right]^T$. The input joint angles are θ_1, θ_2 and φ as indicated in Fig. 5. The forward kinematic analysis concerns with the determination of the end-effector's position corresponding to given joint angles. Based on Fig. 5, the manipulator's loop closure equation can be obtained as:

$$\overline{\boldsymbol{BF}} = \overline{\boldsymbol{BE}} + \overline{\boldsymbol{EF}} \tag{7}$$

where $\overline{\boldsymbol{BF}}$ is the end-effector's position vector ($\boldsymbol{P_f}$). From Eq. (7), the three components of the end-effector's position can be obtained as:

$$x_f = \mathbb{b} * (\cos\theta_1 - \cos\theta_2)\cos\varphi \tag{8}$$

$$y_f = \mathbb{b} * (\cos\theta_1 - \cos\theta_2)\sin\varphi \tag{9}$$

$$z_f = \mathbb{b} * (\sin\theta_1 - \sin\theta_2) \tag{10}$$

So, by using Eqs. (8) - (10), the end-effector's location can be obtained easily with regard to the fixed frame {o-xyz} with known values of joint angles θ_1, θ_2, and φ and the dimensional parameter $\mathbb{b}$.

B. INVERSE KINEMATIC ANALYSIS

Inverse kinematic analysis of the proposed manipulator concerns with the determination of the joint angles θ_1, θ_2, and φ corresponding to given desired position of the end-effector. The solution of the inverse kinematics can be deducted from Eqs. (8) - (10). These non-linear equations have four solutions for θ_1, θ_2, and φ. The correct solution that corresponds to the proposed manipulator's configuration is shown below:

$$Q_1 = x_f^2 + y_f^2 + z_f^2 \tag{11}$$

$$Q_2 = (-Q_1(-y_f^2 + Q_1)(-4\mathbb{b}^2 + Q_1)) \tag{12}$$

$$\theta_1 = \text{atan2}\left(\frac{\sqrt{Q}_2 + Q_1 y_f}{\mathbb{b}Q_1}, \frac{\sqrt{Q}_2 y_f + Q_1(-y_f^2 + Q_1)}{\sqrt{\frac{1}{-y_f^2+Q_1}}\mathbb{b}Q_1(-y_f^2 + Q_1)}\right) \tag{13}$$

$$\theta_2 = \text{atan2}\left(\frac{\sqrt{Q}_2 - Q_1 y_f}{2\mathbb{b}Q_1}, -\frac{\sqrt{Q}_2 y_f + Q_1(-y_f^2 + Q_1)}{2\sqrt{\frac{1}{-y_f^2+Q_1}}\mathbb{b}Q_1(-y_f^2 + Q_1)}\right) \tag{14}$$

$$\varphi = \text{atan2}\left(-z_f\sqrt{\frac{1}{-y_f^2 + Q_1}}, x_f\sqrt{\frac{1}{-y_f^2 + Q_1}}\right) \tag{15}$$

C. FORWARD VELOCITY KINEMATIC ANALYSIS

By taking the derivative of the forward kinematic Eqs. (8) - (10), the velocity kinematic equations can be determined as:

$$\begin{bmatrix} \dot{x}_f \\ \dot{y}_f \\ \dot{z}_f \end{bmatrix} = \begin{bmatrix} -\mathbb{b}\cos\varphi\sin\theta_1 & \mathbb{b}\cos\varphi\sin\theta_2 & -\mathbb{b}\sin\varphi\,(\cos\theta_1-\cos\theta_2) \\ \mathbb{b}\sin\varphi\sin\theta_1 & -\mathbb{b}\sin\varphi\sin\theta_2 & -\mathbb{b}\cos\varphi\,(\cos\theta_1-\cos\theta_2) \\ \mathbb{b}\cos\theta_1 & -\mathbb{b}\cos\theta_2 & 0 \end{bmatrix} \begin{bmatrix} \dot{\theta}_1 \\ \dot{\theta}_2 \\ \dot{\varphi} \end{bmatrix} = J \begin{bmatrix} \dot{\theta}_1 \\ \dot{\theta}_2 \\ \dot{\varphi} \end{bmatrix} \tag{16}$$

where J stands for the Jacobian matrix.

D. INVERSE VELOCITY KINEMATIC ANALYSIS

The inverse velocity kinematic equations can be determined by taking the inverse of the Jacobian matrix in Eq. (16) as follows:

$$\begin{bmatrix} \dot{\theta}_1 \\ \dot{\theta}_2 \\ \dot{\varphi} \end{bmatrix} = \begin{bmatrix} \frac{\cos\varphi\cos\theta_2}{\mathbb{b}\sin(\theta_2-\theta_1)} & \frac{-\sin\varphi\cos\theta_2}{\mathbb{b}\sin(\theta_2-\theta_1)} & \frac{\sin\theta_2}{\mathbb{b}\sin(\theta_2-\theta_1)} \\ \frac{\cos\varphi\cos\theta_1}{\mathbb{b}\sin(\theta_2-\theta_1)} & \frac{-\sin\varphi\cos\theta_1}{\mathbb{b}\sin(\theta_2-\theta_1)} & \frac{\sin\theta_1}{\mathbb{b}\sin(\theta_2-\theta_1)} \\ \frac{-\sin\varphi}{\mathbb{b}(cos\theta_1-\cos\theta_2)} & \frac{-\cos\varphi}{\mathbb{b}(cos\theta_1-\cos\theta_2)} & 0 \end{bmatrix} \begin{bmatrix} \dot{x}_f \\ \dot{y}_f \\ \dot{z}_f \end{bmatrix} = J^{-1} \begin{bmatrix} \dot{x}_f \\ \dot{y}_f \\ \dot{z}_f \end{bmatrix} \tag{17}$$

where J^{-1} stands for the Jacobian inverse matrix.

V. WORKSPACE ANALYSIS

Based on the schematic diagram shown in Fig. 5, point F reaches the boundary of the workspace at the full stretch configuration of the manipulator. This configuration can be obtained when $\psi = 180^o$, i.e. when $\theta_2 = 180^o + \theta_1$. By substituting in the forward kinematic Eqs. (8) - (10), the end-effector's position at the boundary of the workspace is found to be as follows:

$$x_f = 2\mathbb{b}\cos\theta_1\cos\varphi \tag{18}$$
$$y_f = -2\mathbb{b}\cos\theta_1\sin\varphi \tag{19}$$
$$z_f = 2\mathbb{b}\sin\theta_1 \tag{20}$$

Squaring both sides of Eqs. (18) - (20) and adding together to eliminate the angles, one gets the workspace equation as follows:

$$\frac{x_f^2}{(2\mathbb{b})^2} + \frac{y_f^2}{(2\mathbb{b})^2} + \frac{z_f^2}{(2\mathbb{b})^2} = 1 \tag{21}$$

So, from Eq. (21), the workspace is a hemisphere with a radius equals to $(2\mathbb{b})$ which equals to the manipulator's reach.

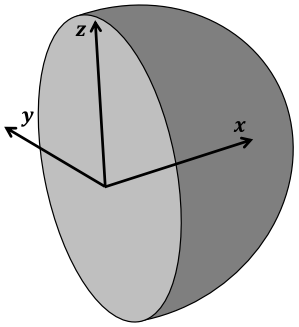

FIGURE 8. The total workspace of the proposed manipulator.

Fig. 8 displays the workspace shape of the proposed manipulator as a hemisphere. So, the workspace volume can be obtained as a function of the dimensional parameter ($\mathbb{b}$) as follows:

$$V = \frac{2}{3}\pi\,(2\mathbb{b})^3 \tag{22}$$

Using Lagrange Multiplier Theorem, the maximum workspace volume of the proposed manipulator can be calculated as follows:
Maximize:

$$f\,(x, y, z) = V = 4xyz \tag{23}$$

Subject to:

$$g\,(x, y, z) = \frac{x_f^2}{(2\mathbb{b})^2} + \frac{y_f^2}{(2\mathbb{b})^2} + \frac{z_f^2}{(2\mathbb{b})^2} - 1 = 0 \tag{24}$$

Lagrange function L is defined as:

$$L = 4xyz + u\left(\frac{x_f^2}{(2\mathbb{b})^2} + \frac{y_f^2}{(2\mathbb{b})^2} + \frac{z_f^2}{(2\mathbb{b})^2} - 1\right) \tag{25}$$

where u stands for Lagrange Multiplier. So, the necessary conditions according to Lagrange Theorem treating x, y, z and u as unknowns are obtained as follows:

$$\frac{\partial L}{\partial x} = 4yz + \frac{2ux}{4b^2} = 0 \tag{26}$$
$$\frac{\partial L}{\partial y} = 4xz + \frac{2uy}{4b^2} = 0 \tag{27}$$
$$\frac{\partial L}{\partial z} = 4xy + \frac{2uz}{4b^2} = 0 \tag{28}$$
$$\frac{\partial L}{\partial u} = \frac{x_f^2}{(2\mathbb{b})^2} + \frac{y_f^2}{(2\mathbb{b})^2} + \frac{z_f^2}{(2\mathbb{b})^2} = 1 \tag{29}$$

By solving Eqs. (26)-(29), one can get all workspace dimensional parameters as follows:

$$x = y = z = \frac{2}{\sqrt{3}}\mathbb{b} \tag{30}$$

By making a comparison between the proposed manipulator and the 3D pantograph manipulator taking into account the same dimensional parameter of the 3D pantograph manipulator as $\mathbb{b} = 475$ mm [27]. The calculated cuboid volume of

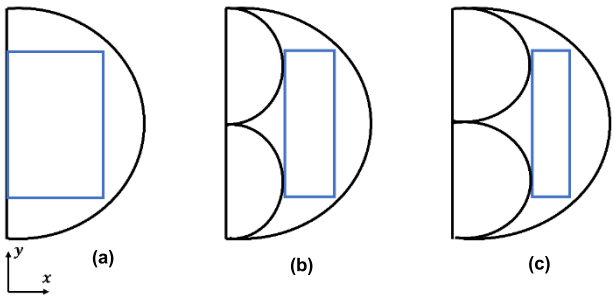

FIGURE 9. Comparison between the maximum cuboid volume of (a) The proposed interconnected manipulator without internal singularities (b) The proposed manipulator before modifications to eliminate internal singularities [36]. (c) The 3D pantograph manipulator [27].

the proposed manipulator will be about 0.33 m^3 in the case of internal singularities [36].

So, the workspace volume of the proposed manipulator after eliminating all internal singularities is equal to 3 times of the workspace volume of the 3D pantograph manipulator and 9 times of the pantopteron workspace volume. Fig. 9 shows a comparison between the maximum cuboid volume of three manipulators namely; a) the proposed manipulator after eliminating internal singularities, b) the proposed manipulator before eliminating internal singularities, and c) the 3D pantograph manipulator.

The calculated cuboid volume after eliminating all internal singularities for the final version of the proposed manipulator will be about 0.66 m^3. As indicated in [27], the 3D pantograph manipulator has a workspace volume equal to 0.228 m^3 that is equal to 3 times of the workspace volume of the pantopteron robot [24] with the same dimensional parameter.

VI. MECHANICAL DESIGN

In order to evaluate the mechanical properties of a potentially manufacturable hardware structure, we built the mechanical model of our proposed system as shown in Fig. 10. Here, the drive system uses three rotary motors installed at/near the fixed base. The motors **a** and **b** enable to control the angles θ_1 and θ_2 and are attached with timing belts and pulleys to drive the joint shafts. Motor **c** enable to control the angle φ and is attached with spiral bevel gears to drive the joint shaft.

Fig. 10 shows the proposed manipulator with its balance system and driving system including the timing belt and bevel gears. Also, the end-effector is attached with a suction cup head as to be used in some industrial applications. The designed balancing system to minimize the power consumption which will be presented in subsection VI (B) is shown in Fig. 11. It consists of a combination of extension springs with cables-pulleys arrangement. The third timing belt shown in Figs 10 and 11 is used for adjusting the balancing of the manipulator using a small balancing weight practically as the calculations provides approximate values for gravity compensation.

Also, the proposed manipulator can be utilized in the applications that need changing the end-effector orientation

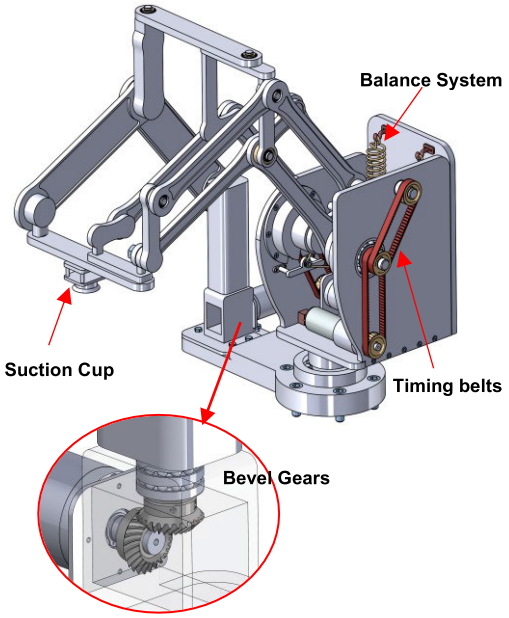

FIGURE 10. The 3D CAD model of the proposed interconnected manipulator with driving and balance system.

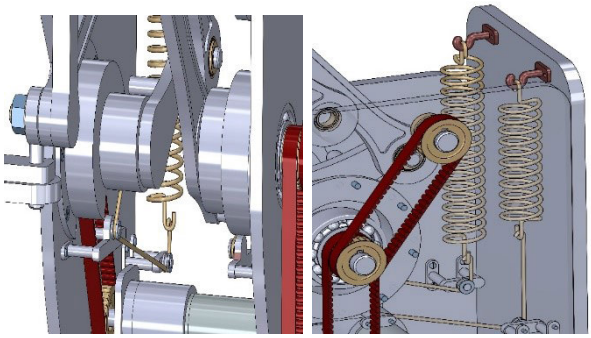

FIGURE 11. The balancing system of the proposed interconnected manipulator.

through occupying it with a spherical wrist which increases the manipulator's degrees of freedom to six as shown in Fig. 12(a).

Consequently, the end-effector's orientation does not depend on its position which reduces power consumption and simplifies the planning process. This is in contrary to most serial manipulators. In addition, it is possible to use a rotary base and a spherical wrist in the end-effector to seamlessly increase the degrees of freedom by 4 (1 due to the rotary base, and 3 due to the rotations of the spherical wrist) which increases the degrees of freedom of the proposed manipulator to seven as shown in Fig. 12(b)&(c).

The advantages of the proposed translational robot over existing translational robots are its combined serial and parallel advantages (high workspace-to-size ratio, speed, accuracy and rigidity) achieved using three rotary actuators that none of the existing translational robots have. Comparing to delta robot as example, the proposed robot has much higher workspace-to-size ratio than that of the delta robot while

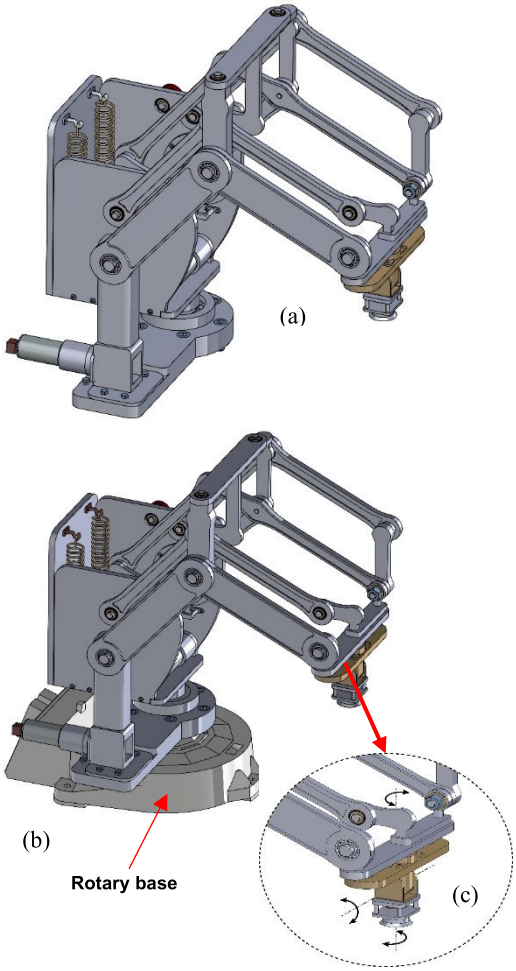

FIGURE 12. The proposed Interconnected Manipulator with (a) 6 DOF, (b) 7 DOF. (c) Spherical wrist with its axes and a suction cup attached to it.

possesses speed, accuracy and rigidity comparable to those of the delta robot.

The applications of the proposed robot are pick and place operations, palletizing, automatic welding, automatic painting, assembly and packaging.

A. STRESS AND DEFORMATION ANALYSIS

To evaluate both strength and rigidity characteristics, for simplicity and without loss of performance, we used the I-section for all links due to favorable benefits in stiffness and low weight. In particular, we use the I-section dimensions stipulated at Fig. 15-(a) with $L_1 = 18$ mm, $L_2 = 50$ mm, $t_1 = 13$ mm and $t_2 = 10$ mm; and material properties involving Young's Modulus of 200 GPa, yield strength of 250 MPa, Poisson ratio of 0.266, and density of 7860 kg/m^3. To further increase the torsional stiffness of the manipulator, links (11) and (12) in Fig. 1 use the larger I-section with $L_1 = 18$ mm, $L_2 = 110$ mm, $t_1 = 6$ mm and $t_2 = 4$ mm. Fine tuning of the above-mentioned parameters is out of the scope of this paper.

The finite element analysis was carried out using Ansys©software R3 2019 with the Von Mises stress analysis selected as the failure criterion and the model type is linear elastic isotropic. The proposed manipulator's model is imported to the FEA software after CAD design. The finite element analysis solution started after applying meshing specifications, materials, constraints, external forces (5kg at the end-effector), Gravity forces, connections and joints.

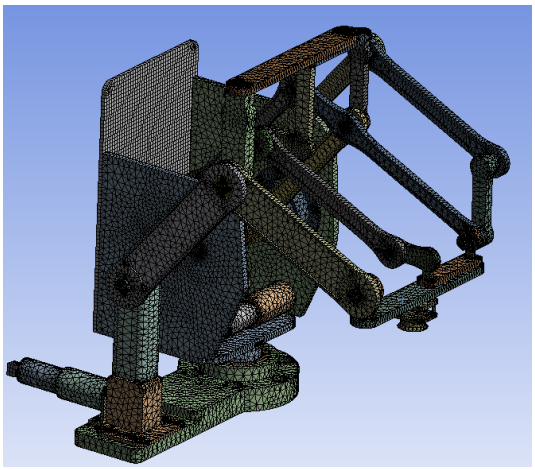

FIGURE 13. Meshing of the proposed robot.

Finite element analysis is performed to evaluate both strength and rigidity under maximum payload of 5 kg, which is suitable for practical and general-purpose manipulations of sorting and picking.

The meshing element is a ten nodal tetrahedron with size equal to 10 mm. the meshing smoothing is medium and the minimum edge length for the element is about 1.3044e-002 mm. The inflation transition ratio is about 0.272. The total number of nodes is 717840 and the total number of elements is 378455. The meshing of the proposed manipulator is shown in figure 13.

The simulation analysis started to calculate the maximum Von-Mises stresses and deformation under the specified conditions as shown in figure 14.

Stress and deformation were calculated at 7 critical points of the available cuboid workspace, as shown by Fig. 15-(b), whose location are expected to attain the maximum deflection and stress. Here, the corner points 1 to 4 in Fig. 15- (b) are located at the boundary of the workspace where singularity occurs. The obtained values in stress and deflection at the above-mentioned critical points are shown in Table 1.

The obtained maximum stress is 54.5 MPa which is much smaller than the yield strength of the material (250 MPa). The maximum deflection is 0.629 mm which is reasonable from the viewpoint of general-purpose manipulations in sorting and picking.

Another configuration of our proposed manipulator considers the longitudinal axis (x-axis) becoming the vertical direction as shown by Fig. 15-(c). This configuration is suitable in applications which need a larger workspace in the horizontal directions (y and z directions) and smaller workspace in the vertical direction (x direction). We also conducted

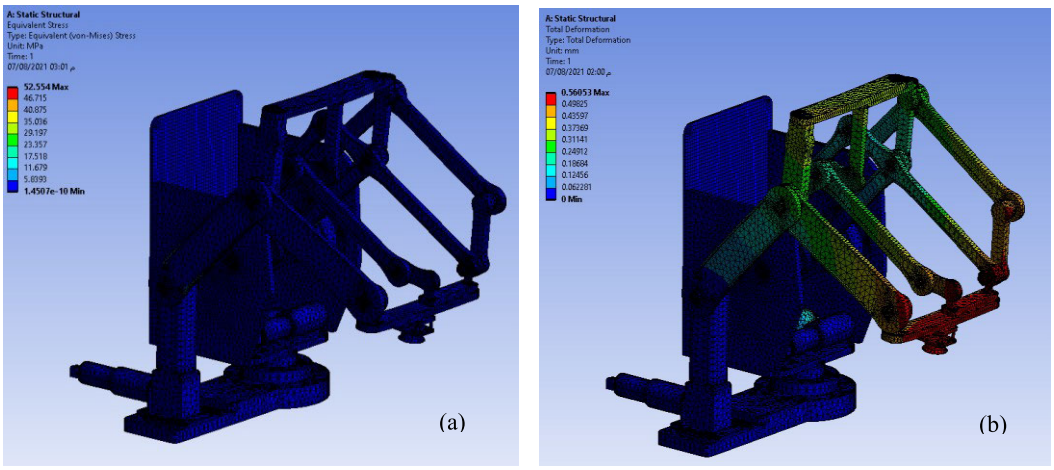

FIGURE 14. FEA of the proposed manipulator (a) Von misses stress analysis, (b) Deformation analysis.

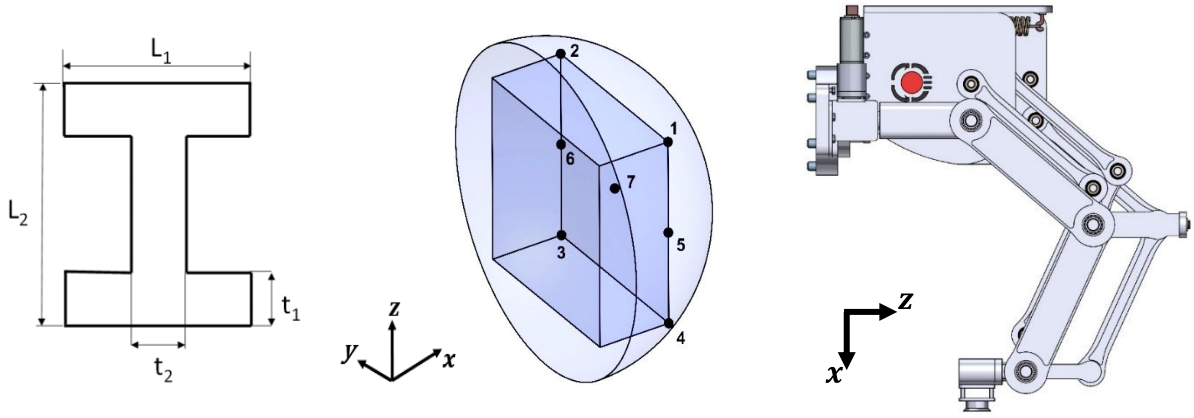

(a) I-section parameters. (b) The cuboid workspace. (c) Setup as parallel manipulator.

FIGURE 15. Elements in stress and deformation analysis.

TABLE 1. The resulted stresses and deflections of the critical points.

Point	Stress (MPa)	Total deflection (mm)	Deflection's components		
			x	y	z
1	54.5	0.629	0.216	0.289	-0.515
2	50.4	0.506	0.259	-0.217	-0.377
3	42.9	0.624	0.346	-0.262	-0.449
4	52.6	0.566	0.188	0.326	-0.424
5	50.8	0.492	0.0629	0.105	-0.476
6	52.6	0.512	0.104	-0.087	-0.494
7	22	0.355	0.292	0.048	-0.197

stress and deformation analysis in the above-mentioned configuration (Fig. 15-(c)). We obtained the maximum stress to be equal to 42.7 MPa, which is much smaller than the yield strength of the considered material (250 MPa).

Also, we found that the maximum deflection was 0.668 mm with components in the x, y and z axis being 0.567, 0.117 and −0.335, respectively. This value is also less than 1 mm under the applied payload (5 kg), which is reasonable from the viewpoint of manipulations in sorting and picking. It is to be noted that the system rigidity can be increased and the system weight can be decreased using optimization techniques which will be carried out in the future work.

Previous studies considered the effect of joint clearance, machining errors and assembly errors for mechanisms and planar manipulators only [37]–[39]. Considering such effects in spatial already known manipulators are very rare and they need a lot of sophisticated analyses [40], [41]. The analysis that is carried out in this paper is needed first to justify the feasibility of the proposed manipulator. Such advanced analysis will be in our agenda for future work.

B. MANIPULATOR BALANCING

The aim of gravity (static) balancing, which we deal with in this work, is to create compensation force for the gravity by using counterweights, springs, pneumatic or hydraulic cylinders, or electromagnetic devices. This will lead to decrease the actuators' torques greatly and hence reduce the power

consumption and the actuators' sizes. This approach differs from the dynamic balance approach which is used to decrease or remove the shaking forces and moments acting on the base to decrease the vibration, noise, wear and fatigue. As a price, the actuators' torques increase. They become double their original values when counter-rotating inertias are used to balance the shaking moments which also complicate the robot structure. This balancing is carried out by conserving the linear and angular momentums (making them constant or zero). In our paper we are not dealing with such balancing approach. For the proposed manipulator, a combination of extension springs with cables-pulleys arrangement is used to balance the overall weight of the working links. There is another approach which uses counterweights to achieve balancing, but this approach increases the inertia of the system and hence increases the power consumption at high-speed applications. The balancing approach starts with the estimation of the balancing masses and their position vectors. This approach is based on equating the total potential energy of the system including that of the balancing masses to a constant. Then one can easily replace the balancing masses by springs & cables-pulleys arrangement that leads to the same static balancing using simple equilibrium equations. However, the proposed manipulator consists of many links. In practice, the mass-centers of these links may not be located on the corresponding joints-lines. This leads to a complicated analytical expression which is difficult to be handled.

Therefore, we propose an alternative approach in which the manipulator is replaced by equivalent rotating-masses systems. The static balancing of these equivalent systems results in the same balancing masses with their locations of the original manipulator. Static balancing of rotating-masses system is much easier than equating the total potential energy to a constant. It can be even carried out numerically. The input torque associated with angle φ does not participate in counteracting the moments produced by the links' weights. So, only the torques associated with angles θ_1 and θ_2 counteract the moments of the links' weights.

In the proposed balancing approach, there are two rotating-masses systems. The first one rotates with $\dot{\theta_1}$ while the second one rotates with $\dot{\theta_2}$. If the vertical position of the mass-center of a link is function of one angle (θ_1 or θ_2), then its mass is included in the corresponding rotating-masses system that rotates with the link angular-velocity $\dot{\theta_1}$ or $\dot{\theta_2}$. If the vertical position of the mass-center of a link is function of both angles (θ_1 and θ_2), then its mass is included in both rotating-masses systems. The balancing of the first rotating-masses system that rotates with $\dot{\theta_1}$ ensures that the part of the potential energy of the manipulator associated with θ_1 is constant. Similarly, the balancing of the second rotating-masses system that rotates with $\dot{\theta_2}$ ensures that the part of the potential energy of the manipulator associated with θ_2 is also constant.

Since the total potential energy of the manipulator consists of these two parts, then the balancing of the two rotating-masses systems ensures the constancy of the total potential energy of the manipulator. There are three types of links in the proposed manipulator. The first type is connected directly to the joints on the rotating base (A, B, N, and G in Fig. 3) such as links 1, 3, and 11 in Fig. 1. The joints on the rotating base are named base-joints. The second type is not connected directly to the base-joints but is connected through another link. The links of the second type are links 2, 4, 6, 8, 12, 19, and 20 in Fig. 1. The third type is the links that have translational motion such as links 7, 9, 13, 14, 15 and 17. Each link in the first and second types has two angles. The first link-angle can be θ_1 or θ_2 according to the link inclination.

The second link-angle is the angle of a line connected the mass center of the link with the closest link-joint to the manipulator-base (θ_{mi}). The length of this line is denoted by r. For example, the first link-angle of link ML in Fig. 3 is θ_2 while the second link-angle is the angle of a line connecting the mass center of link ML with joint M. Also, the first link-angle of link DEF in Fig. 3 is θ_2 while the second link-angle is the angle of a line connecting the mass center of link DEF with joint E.

The first rotating system consists of three groups of masses. The first group contains the masses of the links belong to the first links-type that incline with angle θ_1. The arms of these masses are the corresponding lengths r while the arm angles are the corresponding second link-angles. The second group contains the masses of the links belong to the second links-type for which the links connected them to the base-joints are inclined with angle θ_1. The arms of these masses have length $\mathbb{b}$ while their angles are θ_1. The third group contains the masses of the translating links. The arms of these masses have length $\mathbb{b}$ while their angles are θ_1. Fig. 16(a) represents the first rotating-masses system.

The second rotating system consists of three groups of masses. The first group contains the masses of the links belong to the first links-type that incline with angle θ_2. The arms of these masses are the corresponding lengths r while the arm angles are the corresponding second link-angles. The second group contains the masses of the links belong to the second links-type for which the links connected them to the base-joints are inclined with angle θ_2. The arms of these masses have length $\mathbb{a}$ while their angles are θ_2. The third group contains the masses of the translating links that are connecting to the base-joints through links inclined with angle θ_2. The arms of these masses have length $\mathbb{b}$ while their angles are θ_2+180^{o}. Fig. 16(b) represents the second rotating-masses system.

The static balancing of these two rotating systems produces two balancing masses with their balancing arms as well as the two balancing angles. The balancing angles can be expressed as $\theta_{b1,2} = \theta_{1,2} + \delta_{1,2}$. Where $\delta_{1,2}$ has constant value and is used to attach the balancing mass to a link incline with angle $\theta_{1,2}$ and is attached directly to the driving joint θ_1 or θ_2. To replace these balancing masses with balancing springs & cables-pulley arrangements, we add 180^{o} to $\theta_{b1,2}$ and use it with the resulted balancing mass and arm in the following.

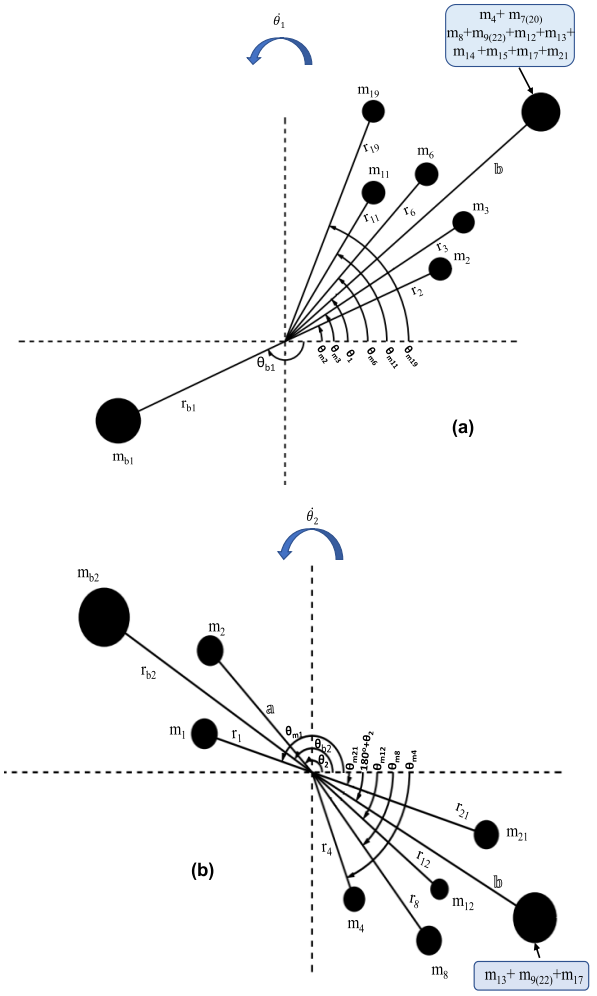

FIGURE 16. Schematic diagram of (a) the first rotating mass system (b) the second rotating mass system.

The extension spring is attached to the driver's link as shown in Fig. 17. The main idea of this approach is to balance the gravitational forces with the moment of the elastic force of the spring [42] as illustrated in Eq. (31):

$$m_b * g * s * \sin(\beta) = F_{sp} * a * \frac{r'}{l_{AB}} * sin(\beta) \qquad (31)$$

where m_b is the equivalent balancing mass, s is the arm of the balancing mass, β is the angle between the arm and the vertical axis OB which equals to $\theta_b + 90^o$, F_{sp} is the spring force, a is the distance on the vertical axis between the center of rotation and the center of the pulley on the vertical axis, r' stands for the distance between the center of rotation and the installation point of the spring cable and l_{AB} is the distance between the installation point of the spring cable and the center of the pulley on the vertical axis. The spring force F_{sp} is calculated as follows:

$$F_{sp} = k * l_{AB} \qquad (32)$$

where l_{AB} is equal to the spring deformation and k is the spring stiffness. By substituting in Eq. (31), one obtains:

$$k = m_b * g * \frac{s}{a * r'} \qquad (33)$$

So, one can design the two balancing springs based on the estimated stiffness, Eq. (33), and the maximum spring force. To evaluate the mentioned balancing approach, we used simulations in ADAMS® software considering the dynamics of the manipulator and angle-trajectories of angles φ, θ_1 and θ_2 derived from a quintic polynomial as inputs.

Fig. 18 shows the resulted actuation torques for angles φ, θ_1 and θ_2 with and without the balancing notion. By observing Fig. 18, we note the following facts:

- The torque of angle φ is the same in scenario with and without using the balancing concept. This is due to the torque associated with φ does not counteract the gravitational forces of the manipulator-links.
- The maximum torque of angle θ_1 and θ_2 is about 108 Nm (64 Nm) without the balancing system, and is reduced to 0.46 Nm (0.125 Nm) with a reduction ratio of 234 (512) times owing to the balancing system.

Hence, the results show that the balancing system reduces significantly the actuation torques associated with θ_1 and θ_2 being potential to enable the use of small-sized motors.

VII. SIMULATION EXPERIMENTS

In order to evaluate the performance in control settings, which is relevant to sorting and picking manipulations in general-purpose settings, we implemented a PID controller and evaluated its performance.

Basically, we used ADAMS® software, being relevant to consider the nonlinear dynamics of the manipulator. For control experiments, we used the co-simulation between ADAMS® software and MATLAB/Simulink®.

Then, our virtual environment consists of the following elements:

- For simplicity and without loss of generality, we used trajectory rendered from a fifth-order quintic polynomial to move the end-effector in the x, y and z directions.
- Then, a user-defined trajectory becomes the inputs to the
- system of inverse kinematics, which is able to generate the desired trajectories associated to the joint angles of the rotary actuators.
- The difference between the desired values of joint angle and the corresponding measured values obtained from the simulation model in ADAMS become the input errors to the PID controller as shown in Fig. 16.
- The performance of trajectory tracking of the proposed manipulator is evaluated under a 5 kg payload applied to the end-effector.

The manipulator's model was imported from CAD software with accurate dimensions and assembly. This model was imported into ADAMS® with joints and actuators applied accurately. Then, using control options in ADAMS®,

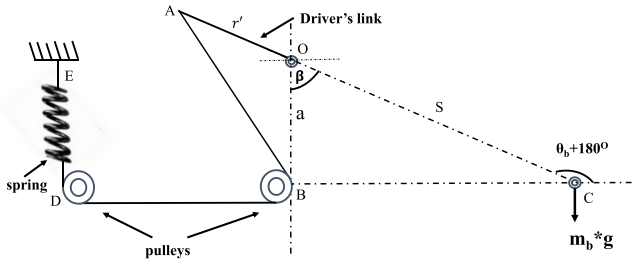

FIGURE 17. Gravity compensation of a rotating link using extension springs.

the system was exported as a block in MATLAB®/Simulink. ADAMS®-exported model contains all relevant information to be used in the PID control scheme (Figure 19), where the balancing is denoted by gravity compensation (GC) components (as described in section VI-B and Figure 18). The controlled torques are calculated in MATLAB/Simulink and delivered as inputs to the ADAMS model. The ADAMS model produces the current angles of the active joints which are used as inputs to the controller in MATLAB/Simulink. The controller subtracts these measured angles from the reference angles as shown in Figure 19-20 calculated from the inverse kinematic equations to find the position errors used in the control algorithm. PID control was used in this paper and achieved a high-performance trajectory tracking to operate the proposed manipulator. The authors also tested a RIC control system [43] and the performance was similar to the PID scheme, succeeding at operating the proposed manipulator accurately. Operating the proposed manipulator with a heavy weight and maximum payload with a simple controller is considered an additional merit to the proposed manipulator compared with other industrial robots.

As shown in Fig. 21 (a, b and c), the results confirm that the proposed manipulator can move its end-effector translational motions in the 3D space without changing its orientation. To show the performance of trajectory tracking under the above-mentioned considerations, Fig.22 presents

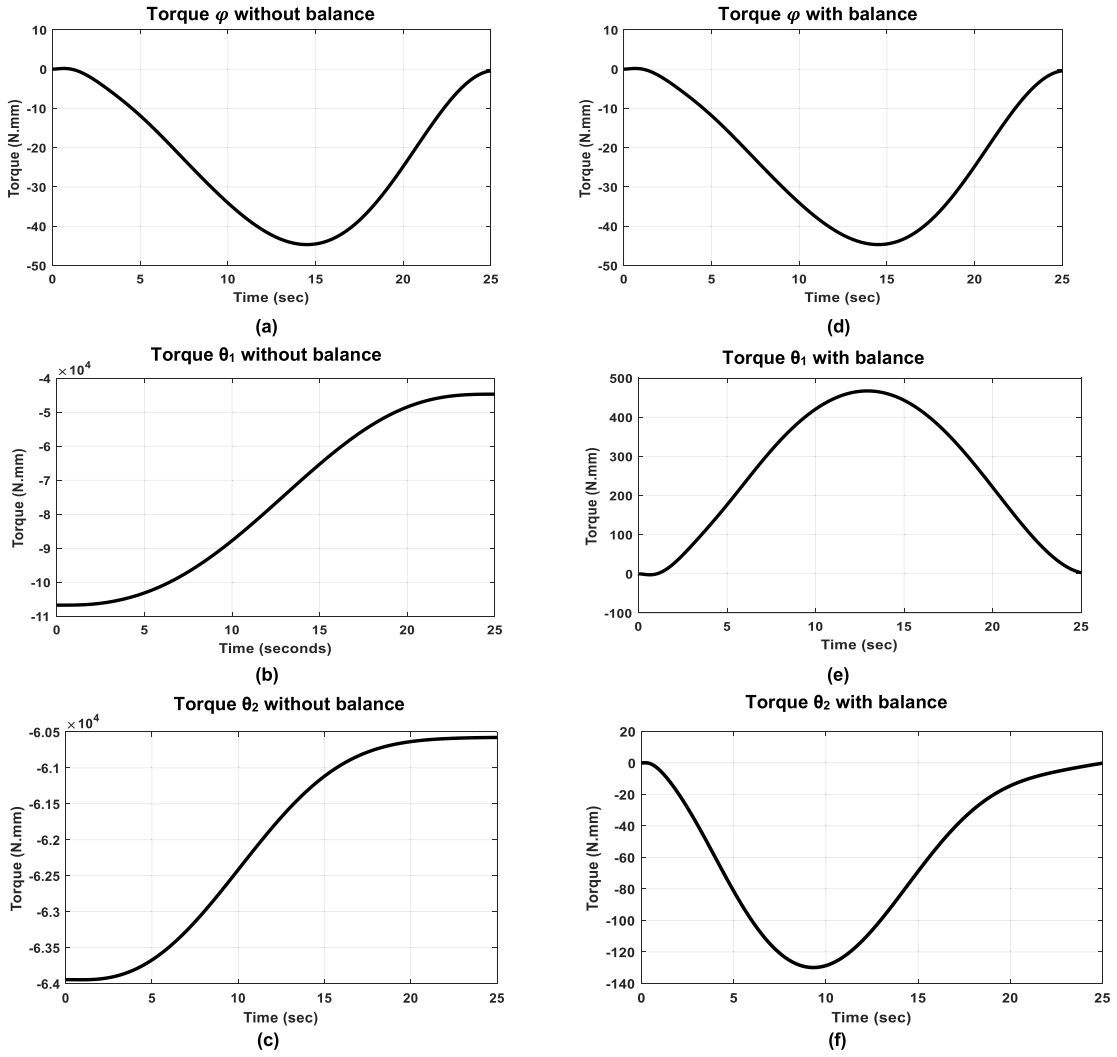

FIGURE 18. The resulted torques of actuators before and after balancing: Figures (a), (b) and (c) show the torques of φ, θ_1 and θ_2 without balancing while Figures (d), (e) and (f) show the torques of φ, θ_1 and θ_2 with balancing.

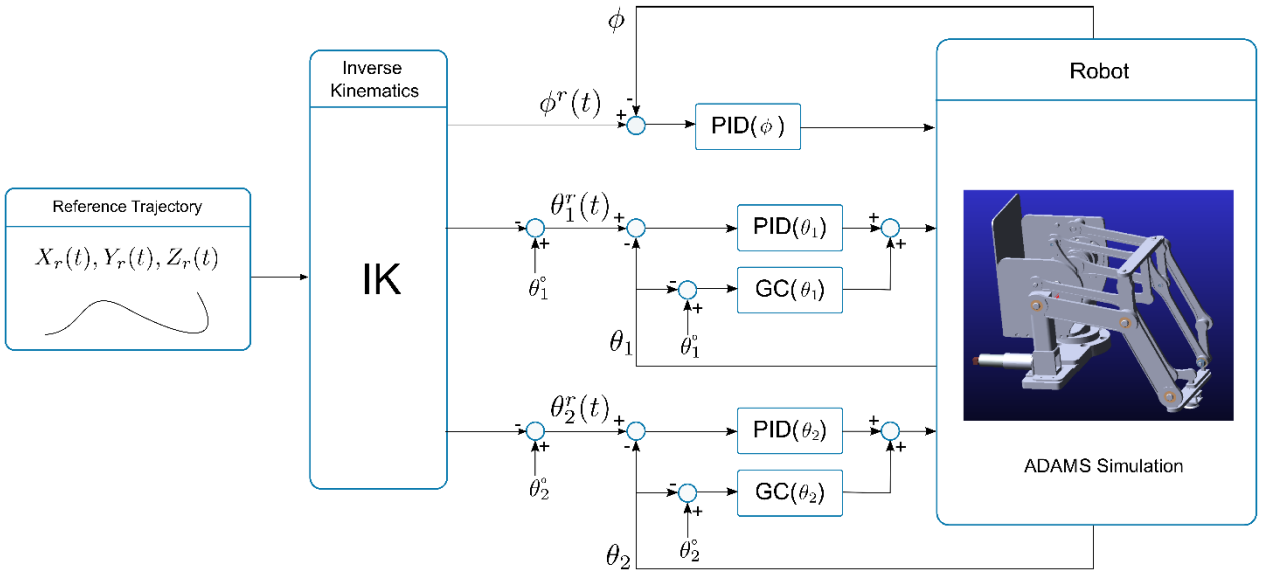

FIGURE 19. Block diagram of the PID control system. Here $\theta_1^\circ = 50^\circ$ and $\theta_2^\circ = 155^\circ$ denote the initial values of angles.

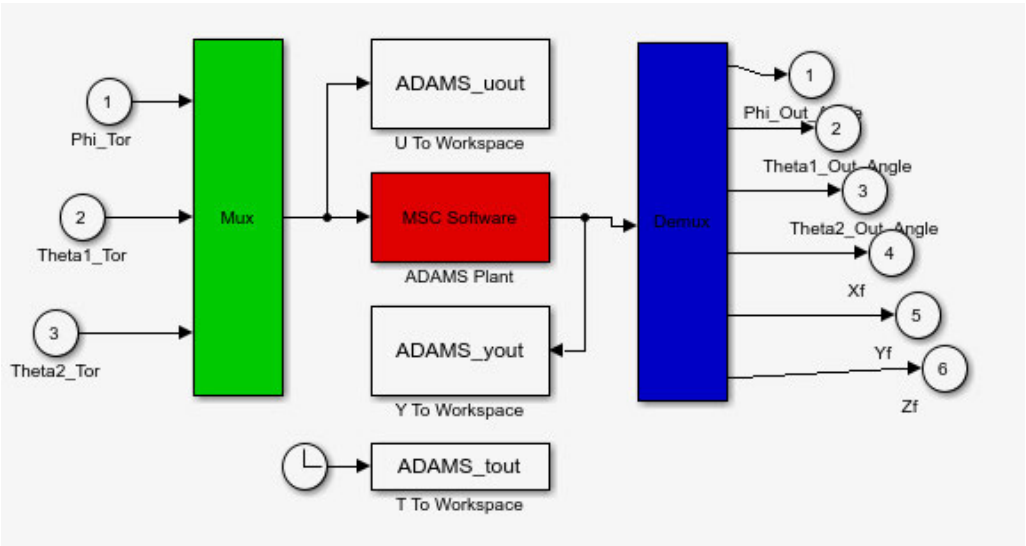

FIGURE 20. ADAMS Model presented in MATLAB/Simulink.

the trajectories of the end-effector in the x, y and z directions, and Fig. 23 presents the performance of tracking angles φ, θ_1 and θ_2. In both Fig. 22 and Fig. 23:

- The x axis denotes the simulation time in seconds.
- The y axis in Fig. 22 denotes the displacement of the end effector in x, y and z directions.
- The y axis in Fig. 23 denotes the value of the angles φ, θ_1 and θ_2.
- The achieved (user-defined) displacement and trajectory is portrayed by blue (red) color.

By observing the results from Fig. 22 and Fig. 23, we note the following facts:

- There is reasonable agreement between the desirable and achieved trajectories of the end-effector and joint angles.
- The tracking performance of all trajectories are satisfactory, implying that the proposed manipulator is seamlessly controlled by the PID controller.

The results confirmed the feasibility of using simple PID control schemes to attain high-performing trajectory tracking of the end-effector. Studying the performance of control and planning schemes for adaptive user-defined scenarios is in our agenda.

The proposed manipulator was compared to a Delta Robot inspired by [44] to evaluate its performance, accuracy, speed, and rigidity in a pick and place task. For fairness of evaluations, the overall size and the cycle geometry for pick and place are assumed to be the same compared to the proposed manipulator. The simulation results show that our system

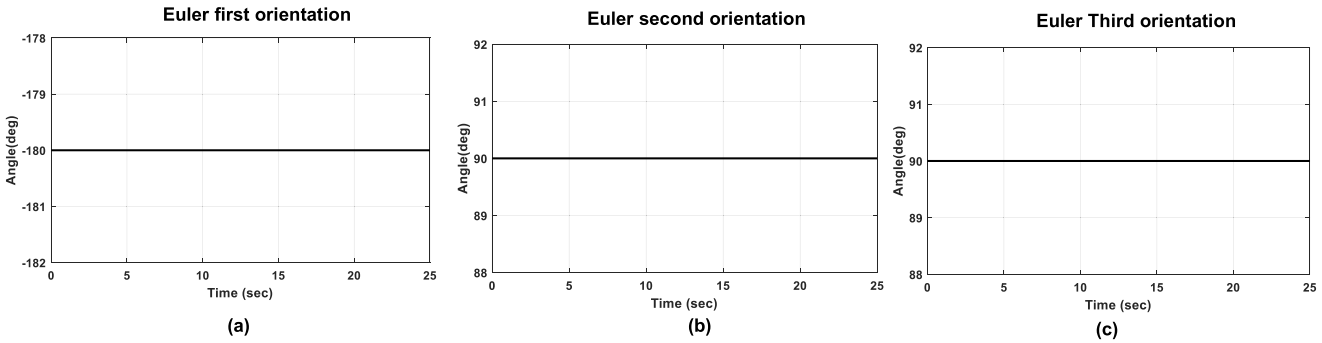

FIGURE 21. Simulation results of the proposed manipulator show the constant orientation of the end-effector in the 3D space. (a) Euler first orientation. (b) Euler second orientation. (c) Euler third orientation.

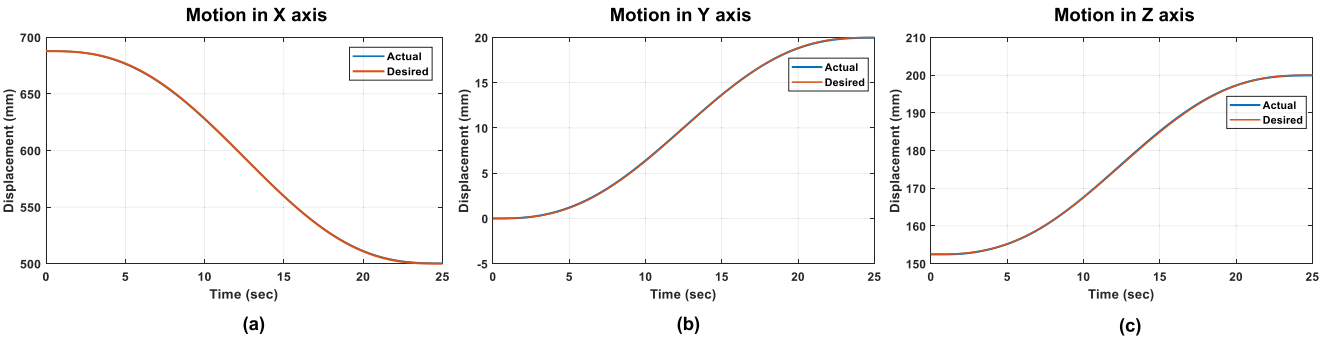

FIGURE 22. Simulation results of the proposed manipulator: trajectory of the end-effector. (a) Motion in X axis. (b) Motion in Y axis. (c) Motion in Z axis.

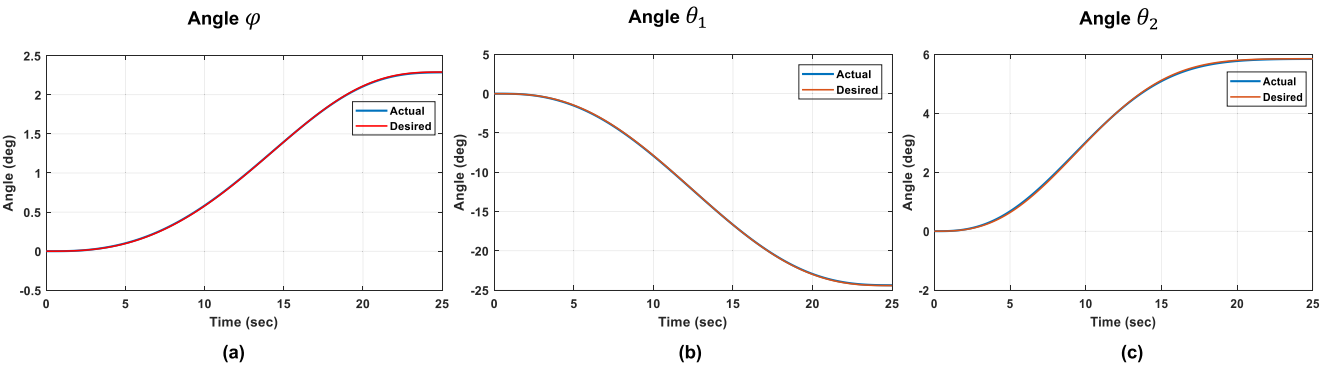

FIGURE 23. Results in angle trajectory tracking. (a) Angle φ. (b) Angle θ_1. (c) Angle θ_2.

can achieve reasonable speed performance comparable to a Delta Robot. Figure 24 and Figure 25 show the pick and place motion of the end-effector in YZ plane, and z axis respectively, depicting the accuracy of the end-effector to follow the desired trajectory in a standard pick and place cycle at the duration of 0.7 seconds at maximum payload of 5kg. Also, another pick and place cycle motion is carried out using a payload of 3kg at the duration of 0.45 seconds like Delta robot as shown in Figures 26 and 27.

The deformation analysis shown in Table 2 reported that our manipulator was more rigid and subject to lower deformation. Also, the stress analysis showed that the proposed manipulator was subject to lower stresses at the same payload as shown below at table 2.

TABLE 2. Comparison between the proposed robot and Delta robot.

	The proposed manipulator	Delta Robot
Maximum Von-misses Stress	54.5 MPa	208 MPa
Maximum Deformation	0.668 mm	0.903 mm
Cycle time of pick and place operation with 3 kg payload	0.45 sec	0.45 sec

We believe our proposed manipulator is potential to further extend the efficiency and economic frontiers of the available industrial robots in the literature, whose realization may find use in general-purpose manipulation tasks such as sorting and

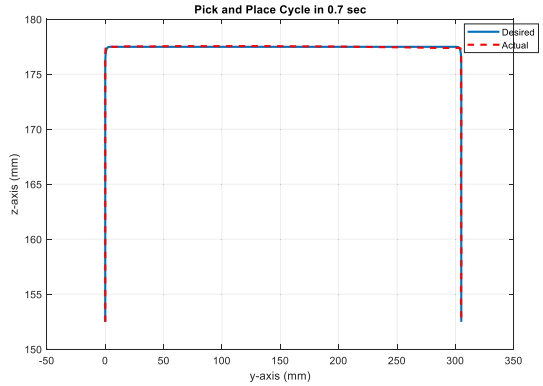

FIGURE 24. Pick and place cycle in YZ plane during 0.7 sec with 5 kg payload.

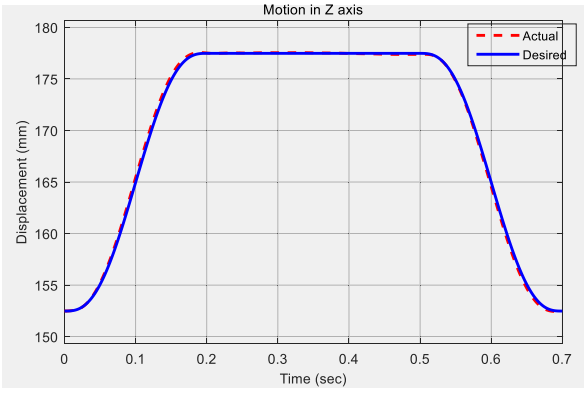

FIGURE 25. Motion in z axis during 0.7 sec with 5 kg payload.

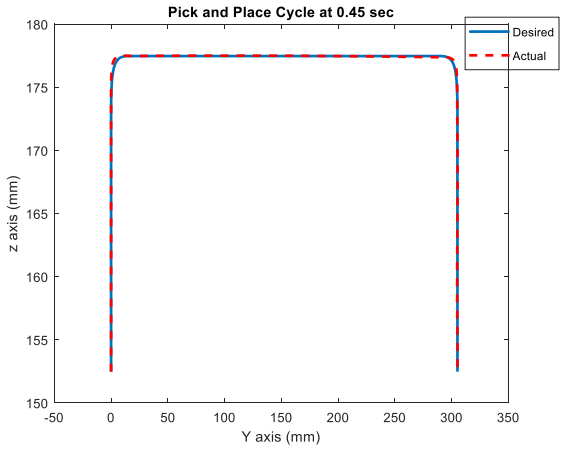

FIGURE 26. Pick and place cycle in YZ plane during 0.45 sec with 3 kg payload.

picking-placing in industrial settings. Finally, the first prototype of the proposed manipulator has been manufactured and assembled as shown in figure 28.

Studying the performance of the manufactured prototype and making further evaluations to compare with other industrial robots are in our agenda as future work to make the necessary improvements.

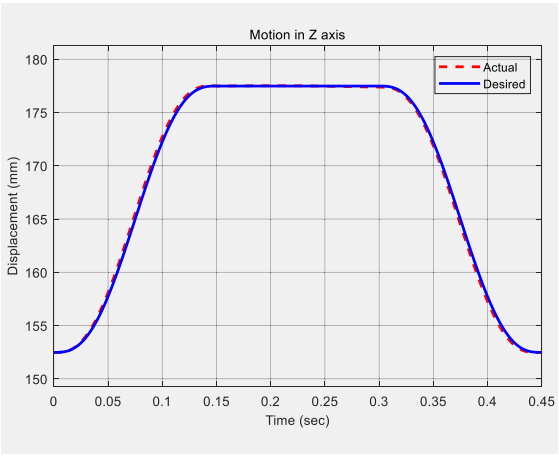

FIGURE 27. Motion in z axis during 0.45 sec with 3 kg payload.

FIGURE 28. The manufactured manipulator.

VIII. CONCLUSION

This paper has proposed a 3D translational interconnected manipulator by using only revolute joints and three rotary actuators. In contrast to the existing manipulators in the literature, the workspace of the proposed manipulator is free from internal singularities.

In contrast to existing serial manipulators in the field, the end-effector with a spherical wrist is able to rotate around the three perpendicular axes where its orientation is independent of its position. By using a suitable method to study the configuration of kinematic mechanisms with geometric constraints, we examined the mobility of our proposed manipulator by sketching the velocity diagrams in 3D domain. We also analytically explored the workspace environment as well as the largest cuboid workspace in 3D domain. We found that the workspace of the proposed manipulator is 3 (9) times larger than that of the 3D pantograph (pantopteron) manipulator.

Finite element analysis is carried out to explore the mechanical characteristics of our manipulator. A potentially manufacturable structure is found to be safe from the viewpoints of stress and deformation analysis under a 5 kg

payload. And, our computational analysis considering the nonlinear dynamics have shown that a tailored balancing system was able to significantly reduce the required torque in the rotary (motor) actuators by a factor of 234 and 512 times, implying the reduced size and power consumption of motors.

Also, we conducted computational experiments based on Furthermore, our computational simulation experiments based on the co-simulation between MATLAB®/Simulink and ADAMS® have shown the feasibility of using simple PID control schemes to attain high-performing trajectory tracking of the end-effector and of the joint angles.

Studying the performance frontiers with regards to rigidity, weight and manufacturing by using topology optimization, as well as examining control and planning schemes for adaptive scenarios is in our agenda.

We believe our proposed scheme is potential to further extend the efficiency and economic frontiers of the available interconnected robots in the literature, whose realization may find use in general-purpose manipulation tasks such as sorting and picking-placing in industrial settings. Finally, the proposed manipulator has been manufactured and assembled.

ACKNOWLEDGMENT

The first author would like to thank the Ministry of Higher Education of Egypt for supporting him with a scholarship to complete this work. Our sincere thanks to Egypt-Japan University of Science and Technology (E-JUST) for guidance and support as well as for the financial support of manufacturing the manipulator prototype together with Agro-Food Alliance. Our Thanks to Waseda University for its guidance and financial support of the publication fees.

REFERENCES

[1] J. Angeles, *Fundamentals of Robotic Mechanical Systems*. Cham, Switzerland: Springer, 2014.
[2] B. Belzile, P. K. Eskandary, and J. Angeles, "Workspace determination and feedback control of a pick-and-place parallel robot: Analysis and experiments," *IEEE Robot. Automat. Lett.*, vol. 5, no. 1, pp. 40–47, Jan. 2020.
[3] G. Wu, S. Caro, and J. Wang, "Design and transmission analysis of an asymmetrical spherical parallel manipulator," *Mechanism Mach. Theory*, vol. 94, pp. 119–131, Dec. 2015.
[4] Y. Hu, F. Gao, X. Zhao, B. Wei, D. Zhao, and Y. Zhao, "Kinematic calibration of a 6-DOF parallel manipulator based on identifiable parameters separation (IPS)," *Mechanism Mach. Theory*, vol. 126, pp. 61–78, Aug. 2018.
[5] Z. Xu, L. Yang, W. Huang, and L. Hu, "Dynamics analysis of a novel 3-PSS parallel robot based on linear motor," *IEEE Access*, vol. 8, pp. 119048–119061, 2020.
[6] Z. Zhang, L. Wang, and Z. Shao, "ImprovingImproving the kinematic performance of a planar 3-RRR parallel manipulator through actuation mode conversion," *Mechanism Mach. Theory*, vol. 130, pp. 86–108, Dec. 2018.
[7] S. Herrero, C. Pinto, O. Altuzarra, and M. Diez, "Analysis of the 2PRU-1PRS 3DOF parallel manipulator: Kinematics, singularities and dynamics," *Robot. Comput.-Integr. Manuf.*, vol. 51, pp. 63–72, Jun. 2018.
[8] L.-W. Tsai, G. C. Walsh, and R. E. Stamper, "Kinematics of a novel three DOF translational platform," in *Proc. IEEE Int. Conf. Robot. Autom.*, vol. 4, Apr. 1996, pp. 3446–3451.
[9] F. Pierrot, C. Reynaud, and A. Fournier, "DELTA: A simple and efficient parallel robot," *Robotica*, vol. 8, no. 2, pp. 105–109, 1990.
[10] A. H. Dastjerdi, M. M. Sheikhi, and M. T. Masouleh, "A complete analytical solution for the dimensional synthesis of 3-DOF delta parallel robot for a prescribed workspace," *Mechanism Mach. Theory*, vol. 153, Nov. 2020, Art. no. 103991.
[11] D. Chablat and P. Wenger, "Architecture optimization of a 3-DOF translational parallel mechanism for machining applications, the orthoglide," *IEEE Trans. Robot. Automat.*, vol. 19, no. 3, pp. 403–410, Jun. 2003.
[12] L.-W. Tsai and S. Joshi, "Kinematics and optimization of a spatial 3-*UPU* parallel manipulator," *J. Mech. Des.*, vol. 122, no. 4, pp. 439–446, 1999.
[13] L.-W. Tsai and S. Joshi, "Kinematic analysis of 3-DOF position mechanisms for use in hybrid kinematic machines," *J. Mech. Des.*, vol. 124, no. 2, pp. 245–253, Jun. 2002.
[14] K. H. Sung and T. Lung-Wen, "Design optimization of a Cartesian parallel manipulator," in *Proc. Int. Design Eng. Tech. Conf. Comput. Inf. Eng. Conf.*, 2002, pp. 865–872.
[15] M. Callegari and M. Tarantini, "Kinematic analysis of a novel translational platform," *J. Mech. Des.*, vol. 125, no. 2, pp. 308–315, Jun. 2003.
[16] W. Liping, X. Huayang, G. Liwen, and Z. Yu, "A novel 3-PUU parallel mechanism and its kinematic issues," *Robot. Comput.-Integr. Manuf.*, vol. 42, pp. 86–102, Dec. 2016.
[17] L. Wang, H. Xu, and L. Guan, "Optimal design of a 3-PUU parallel mechanism with 2R1T DOFs," *Mechanism Mach. Theory*, vol. 114, pp. 190–203, Aug. 2017.
[18] C. M. Gosselin and X. Kong, "Cartesian parallel manipulators," U.S. Patent 20 030 121 351 A1, May 4, 2004.
[19] X. Kong and C. Gosselin, "A class of 3-DOF translational parallel manipulators with linear input-output equations," in *Proc. Workshop Fundam. Issues Future Res. Directions Parallel Mech. Manipulators*, 2002, pp. 25–32.
[20] X. Kong and C. M. Gosselin, *Type Synthesis of Linear Translational rallel Manipulators*. Dordrecht, The Netherlands: Springer, 2002, pp. 453–462.
[21] S. Briot and I. A. Bonev, "Pantopteron: A new fully decoupled 3DOF translational parallel robot for pick-and-place applications," *J. Mech. Robot.*, vol. 1, no. 2, Jan. 2009, Art. no. 021001.
[22] G. Gogu, "Structural synthesis of fully-isotropic parallel robots with Schönflies motions via theory of linear transformations and evolutionary morphology," *Eur. J. Mech.-A/Solids*, vol. 26, no. 2, pp. 242–269, 2007.
[23] B. Bouzgarrou, J.-C. Fauroux, G. Gogu, and Y. Heerah, "Rigidity analysis of T3R1 parallel robot with uncoupled kinematics," in *Proc. 35th Int. Symp. Robot. (ISR)*, Paris, France, Mar. 2004, pp. 1–6.
[24] S. Briot and I. A. Bonev, "Pantopteron-4: A new 3T1R decoupled parallel manipulator for pick-and-place applications," *Mechanism Mach. Theory*, vol. 45, no. 5, pp. 707–721, May 2010.
[25] Q. Zeng, K. F. Ehmann, and J. Cao, "Tri-pyramid robot: Design and kinematic analysis of a 3-DOF translational parallel manipulator," *Robot. Comput.-Integr. Manuf.*, vol. 30, no. 6, pp. 648–657, Dec. 2014.
[26] S. Liao, Q. Zeng, K. F. Ehmann, and J. Cao, "Parameter identification and nonparametric calibration of the tri-pyramid robot," *IEEE/ASME Trans. Mechatronics*, vol. 25, no. 5, pp. 2309–2317, Oct. 2020.
[27] M. Magdy, M. Fanni, A. M. Mohamed, and T. Miyashita, "Kinematic design and novel mobility analysis of a new 3D pantograph decoupled manipulator," *Mechanism Mach. Theory*, vol. 117, pp. 253–275, Nov. 2017.
[28] M. Fanni, M. Magdy, A. Algamal, and M. Lashin, "Novel 3D pantograph translational manipulator," Egypt Patent 518, Mar. 27, 2016.
[29] G. Wu, S. Guo, and S. Bai, "Compliance modeling and error compensation of a 3-parallelogram lightweight robotic arm," in *Recent Advances in Mechanism Design for Robotics*. Cham, Switzerland: Springer, 2015, pp. 325–336.
[30] (2020). *Marchesini, Robocombi*. Accessed: Sep. 9, 2020. [Online]. Available: https://www.marchesini.com/en/machines-lines/robocombi
[31] J. Qi, L. Hao, R. Sun, and J. Xiao, "Study on the mechanism and kinematics of a hybrid robot for blowout preventer assembly," in *Proc. IEEE Int. Conf. Mechatronics Autom.*, Aug. 2014, pp. 1046–1051.
[32] Z.-Y. Li, D.-J. Zhao, and J.-S. Zhao, "Structure synthesis and workspace analysis of a telescopic spraying robot," *Mechanism Mach. Theory*, vol. 133, pp. 295–310, Mar. 2019.
[33] Z. Liu, J. Wu, and D. Wang, "An engineering-oriented motion accuracy fluctuation suppression method of a hybrid spray-painting robot considering dynamics," *Mechanism Mach. Theory*, vol. 131, pp. 62–74, Jan. 2019.
[34] T. K. Tanev, "Geometric algebra based kinematics model and singularity of a hybrid surgical robot," in *Advances in Robot Kinematics 2016*. Cham, Switzerland: Springer, 2018, pp. 431–440.
[35] L. Wang, Z. Zhang, and Z. Shao, "Kinematic performance analysis and promotion of a spatial 3-RPaS parallel manipulator with multiple actuation modes," *J. Mech. Sci. Technol.*, vol. 33, no. 2, pp. 889–902, Feb. 2019.

[36] A. Sameh, M. Fanni, and A. M. Mohamed, "New 3D translational interconnected manipulator for industrial applications," in *Proc. IEEE Int. Conf. Mechatronics Automat. (ICMA)*, Aug. 2018, pp. 469–474.
[37] K.-L. Ting, J. Zhu, and D. Watkins, "The effects of joint clearance on position and orientation deviation of linkages and manipulators," *Mechanism Mach. Theory*, vol. 35, no. 3, pp. 391–401, Mar. 2000.
[38] S. Erkaya and I. Uzmay, "Investigation on effect of joint clearance on dynamics of four-bar mechanism," *Nonlinear Dyn.*, vol. 58, nos. 1–2, pp. 179–198, Oct. 2009.
[39] X. Li-xin and L. Yong-gang, "Investigation of joint clearance effects on the dynamic performance of a planar 2-DOF pick-and-place parallel manipulator," *Robot. Comput.-Integr. Manuf.*, vol. 30, no. 1, pp. 62–73, Feb. 2014.
[40] U. Schneider, M. Drust, M. Ansaloni, C. Lehmann, M. Pellicciari, F. Leali, J. W. Gunnink, and A. Verl, "Improving robotic machining accuracy through experimental error investigation and modular compensation," *Int. J. Adv. Manuf. Technol.*, vol. 85, nos. 1–4, pp. 3–15, Jul. 2016.
[41] A. Chaker, A. Mlika, M. A. Laribi, L. Romdhane, and S. Zeghloul, "Clearance and manufacturing errors' effects on the accuracy of the 3-RCC spherical parallel manipulator," *Eur. J. Mech.-A/Solids*, vol. 37, pp. 86–95, Jan. 2013.
[42] A. Vigen and B. Sébastien, *Balancing of Linkages and Robot Manipulators*. Cham, Switzerland: Springer, 2015.
[43] A. Sameh, M. Fanni, and A. M. Mohamed, "Finite element analysis, control and simulation of a novel 3D hybrid balanced manipulator," *Int. J. Mech. Mechtron. Eng.*, vol. 21, no. 1, pp. 9–19, 2021.
[44] Kawasaki Robotics. *YF003N Robot Specifications*. Accessed: Dec. 15, 2021. [Online]. Available: https://robotics.kawasaki.com/en1/products/robots/pick-place/YF003N

AHMED SAMEH received the bachelor's degree in production and mechanical design engineering and the M.Sc. degree in mechanical design engineering from Mansoura University, in 2008 and 2015, respectively. He is currently pursuing the Ph.D. degree with the Mechatronics and Robotics Engineering Department, Egypt-Japan University of Science and Technology, Egypt. From 2009 to 2015, he worked as a Demonstrator with Mansoura University, where he worked as an Assistant Lecturer, from 2015 to 2017. His research interests include mechanism design of robots, industrial manipulators, modeling, and simulation.

MOHAMED FANNI received the B.E. degree in mechanical engineering from the Faculty of Engineering, Cairo University, in 1981, the M.Sc. degree in mechanical engineering from Mansoura University, Egypt, in 1986, and the Ph.D. degree in engineering from Karlsruhe University, Germany, in 1993. He is currently a Professor with the Department of Mechatronics and Robotics Engineering, Egypt-Japan University of Science and Technology (E-JUST), Alexandria; on leave from the Production Engineering and Mechanical Design Department, Faculty of Engineering, Mansoura University, Egypt. His major research interests include robotics engineering, automatic control, and mechanical design. His current research focuses on design and control of mechatronic systems, surgical manipulators, teleoperation systems, and flying/walking robots.

VICTOR PARQUE (Member, IEEE) received the B.Sc. degree in systems engineering from National Central University, in 2004, the M.B.A. degree from the Graduate School of Business Administration, Esan University, in 2009, and the Ph.D. degree from the Graduate School of Information, Production and Systems, Waseda University, in 2011. He was a Postdoctoral Fellow with the Department of Mechanical Engineering, Toyota Technological Institute, from 2012 to 2014, and an Assistant Professor with Waseda University, from 2014 to 2018, where he is currently an Associate Professor with the Department of Modern Mechanical Engineering. He is also the JSUC Visiting Professor with the Egypt-Japan University of Science and Technology. He is the first author of more than 70 papers in journals, conferences, and book chapters, and is actively involved in research collaborations with both industry and academia. His research interests include principles of learning systems and artificial intelligence and its applications to design engineering, planning, and control. He is a member of IEEE RAS, IEEE IES, IEEE SMC, ACM SIGAI, ACM SIGEVO, the Robotics Society of Japan (RSJ), and the Japan Society for Precision Engineering (JSPE). He was honored as the Finalist in the Hummies Awards for Human-Competitive Results in 2018.

ABDELFATAH M. MOHAMED (Life Senior Member, IEEE) received the Ph.D. degree from the University of Maryland, College Park, USA, in 1990. Since 1990, he has been an Assistant Professor with the Department of Electrical Engineering, Assiut University, Egypt, where he became an Associate Professor in 1995; a Professor in 2000; the Head of the Department of Electrical Engineering, from September 2010 to March 2012; and the Dean of the Faculty of Engineering, from April 2012 to September 2013. From September 1990 to August 1993, he was a Postdoctoral Fellow with the Department of Mechanical Engineering, The University of Texas at Austin, USA. From April 1996 to April 1997, he was a Visiting Professor with the Department of Electrical Engineering, Kanazawa University, Japan. From November 2013 to September 2018, he was the Head of the Department of Mechatronics and Robotics Engineering, Egypt-Japan University of Science and Technology, where he is currently a Professor with the Department of Mechatronics and Robotics Engineering. His research interests include robust and intelligent control, magnetic bearing, magnetic levitation systems, robotics, industrial drives, and power systems.